Processes for the Fabrication of SU-8 Structures and Sputtered Materials on Porous Glass for Electrospray Thruster Manufacturing

by

Catherine J. Nachtigal

B.S., Mechanical Engineering, Rutgers University, 2022

Submitted to the Department of Aeronautics and Astronautics
in partial fulfillment of the requirements for the degree of

MASTER OF SCIENCE IN AERONAUTICS AND ASTRONAUTICS

at the

MASSACHUSETTS INSTITUTE OF TECHNOLOGY

May 2024

Authored by:	Catherine J. Nachtigal Department of Aeronautics and Astronautics May 17, 2024
Certified by:	Paulo C. Lozano M. Alemán-Velasco Professor of Aeronautics and Astronautics, Thesis Supervisor
Accepted by:	Jonathan P. How R. C. Maclaurin Professor of Aeronautics and Astronautics Chair, Graduate Program Committee

Processes for the Fabrication of SU-8 Structures and Sputtered Materials on Porous Glass for Electrospray Thruster Manufacturing

by

Catherine J. Nachtigal

Submitted to the Department of Aeronautics and Astronautics
on May 17, 2024 in partial fulfillment of the requirements for the degree of

MASTER OF SCIENCE IN AERONAUTICS AND ASTRONAUTICS

ABSTRACT

Electrospray thrusters are electric propulsion devices that generate thrust through the use of an electric potential between the emitter, a concentrated point at which a propellant is flowed to, and downstream extractor electrodes that generates a high electric field at the emitter causing the propellant to be accelerated. Current electrospray thruster designs use sharp micron-scale cone-shaped emitters made from porous materials to generate ion emission through passive propellant feeding, but the current design has flaws that affect its lifetime, reliability, and performance. High specific impulse thruster firing occurs when operating in the purely ionic regime (PIR), in which an ionic liquid propellant (a room temperature molten salt or liquid metal) emits individual ions rather than larger droplets. These emitters must be built on the micron-scale to achieve PIR emission, resulting in their operation as large monolithic arrays with a single extractor to produce a usable amount of thrust, such that the failure of one emitter out of thousands could lead to full extractor and device failure. Futher, the broad parameter space (geometry, flow path, insulation, etc) is currently not selected according to the optimal requirements for operation in the PIR. Recent simulations show that PIR emission can be achieved in a relatively narrow domain that depends on the applied electric field, meniscus size, and hydraulic impedance for flat panel capillary emitters. These capillary emitters can be designed with individualized extractors that are connected through a series of fuses, isolating any shortage to a single emitter.

Photolithography is a useful micromanufacturing tool that has not yet been utilized to build solid structures on top of porous structures. This is because a porous substrate would uptake any liquid photoresist applied during fabrication, making the susbtrate lose its porosity. To prevent this, and allow for the formation of solid structures on top of a porous substrate for electrospray thruster applications, this thesis develops a manufacturing plan in which the pores within the substrate are loaded with a volatile organic compound (VOC), allowing a structure to be fabricated on the substrate surface via photolithography, without the material entering the substrate's pores. To regain the substrate's porous structure, the VOC is removed post-manufacturing via sublimation and an acetone wash. Using the manufacturing techniques described in this thesis, a novel electrospray thruster design consisting of capillaries and fuses to optimize PIR performance and prevent shortage propagation is proposed to greatly increase the performance and reliability of electrospray thruster devices.

Thesis supervisor: Paulo C. Lozano
Title: M. Alemán-Velasco Professor of Aeronautics and Astronautics

Acknowledgments

This work could not have been completed without the surplus of support I received throughout this project. First, I would like to thank my advisor, Professor Paulo Lozano. Thank you for taking me on as a graduate student, and not only guiding me through difficult research and experimentation, but also continuously showing excitement, patience, and understanding even when things didn't work. Your enthusiasm and encouragement gave me the determination I needed to persevere.

To all of the graduate students in SPL, thank you for your kindness and assistance. No matter what help I needed between trainings, research guidance, and general venting, you all always made the time to help me in any way that you could. And to all of the MIT.nano staff, particularly Dennis and Kurt, thank you for your guidance and recommendations. Your genuine interest in my work and the time you took to help me problem solve was invaluable to the completion of this project.

To Mom and Anna, thank you for taking every phone call and supporting me states away. And most importantly, to my fiancé Nick, I could not have made it here without you. You believed in me even when I couldn't believe in myself, and your endless love and patience kept me sane and motivated. Thank you for keeping me grounded and never failing to make me laugh.

This work was supported by a NASA Space Technology Graduate Research Opportunity. Thank you for giving me the opportunity to pursue this project, and thank you to my mentor Thomas Liu for always providing excellent guidance and mentorship for this project.

Contents

List of Figures

List of Tables

Chapter 1

Introduction

1.1 Electrospray Thruster Emission

1.1.1 Electric Propulsion Methods

Electric propulsion is defined as utilizing electrical heating and/or electric and magnetic forces in order to accelerate charged species for propulsion. There are three different subcategories in which electric propulsion methods are characterized. These are defined as [1]:

- Electrothermal propulsion. Electricity is used to heat propellant, which is then expanded through a nozzle. Common examples include resistojets, in which the propellant is heated by a heating coil and then passes through an arc discharge in arcjets.

- Electrostatic propulsion. Electricity is used to accelerate propellant ions. Common examples include ion engines, Hall effect thrusters, and electrospray thrusters, which extract ions from the propellant and accelerate them using an applied voltage source.

- Electromagnetic propulsion. Electromagnetic forces are used to accelerate propellant plasma. Common examples include a magnetoplasmadynamic thruster, which ionizes a propellant as it passes through an arc operated between two electrodes within the thruster channel.

Each method of electric propulsion has different strengths and weaknesses correlated with stability, lifetime, efficiency, and power. This thesis will focus on electrospray propulsion, a method of electrostatic propulsion. There are three different electrospray thruster types, which include colloid thrusters, field emission electric propulsion, and ionic liquid ion sources, which vary in the propellant type and particle size used. This thesis will focus on the use of ionic liquid ion sources, as these are the advantageous to use to produce field emission [2]. 1-ethyl-3-methylimidazolium tetrafluoroborate (EMI-BF4) and 1-ethyl-3-methylimidazolium bis(trifluoromethylsulfonyl)imide (EMI-IM) propellants in particular are commonly used ionic liquid propellants, and will be used in this thesis [3].

1.1.2 Electrospray Equations

Electrospray thrusters operate by using an applied voltage to accelerate a propellant, either in a droplet, mixed, or pure ion mode, that is fed through a capillary or to a sharp tip geometry, generally at a passively fed flow rate.

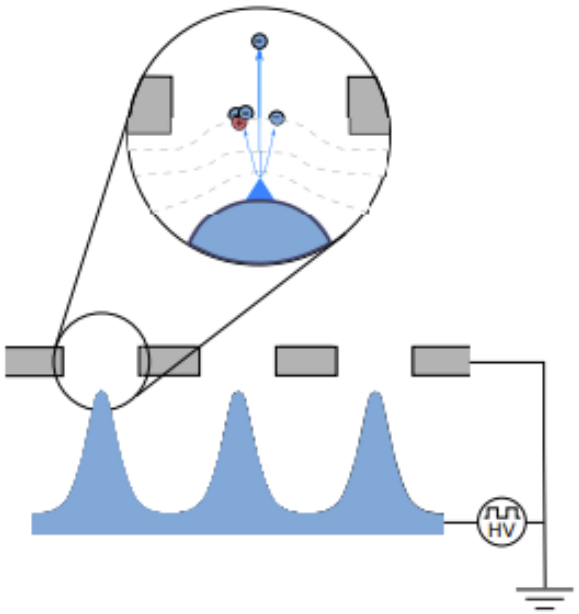

Figure 1.1: Diagram of Electrospray thruster operation [4]

First, the equations describing the droplet emission mode will be discussed. To describe

the characteristics of the thrust plume produced, general electrostatic physics equations may be applied at the emission meniscus region of the electrospray plume. The meniscus is the point at which the ionic liquid propellant is drawn out to a stable point, forming a conical shape as a result of the liquid being polarized through the application of a high voltage potential with respect to a grounded electrode downstream [5]. In the droplet emission mode, it is assumed that there must be a balance between the charge within the droplet and the droplet radius that is emitted from the meniscus [6]. This can be described by Equation 1.1 [7].

$$q = 8\pi r\sqrt{\varepsilon_0 \gamma r} \tag{1.1}$$

Here, q is the Rayleigh instability limit droplet charge, r is the radius, ε_0 is the electric permittivity, γ is the surface tension, and σ is the surface charge density. Equation 1.1 refers to the instability charge at which a higher charge will cause the droplet to disperse into smaller droplets. By dividing this equation by the droplet mass, the maximum charge to mass ratio for the droplet can be obtained, which depends on the radius of the droplet. The radius of the jet can be estimated from the radius of the droplet, and therefore the charge to mass ratio can be estimated from the radius of the jet as well as the flow rate in Equation 1.2 [8].

$$\frac{q}{m} = \frac{6\sqrt{\varepsilon_0 \gamma}}{\rho(1.89R_{jet})^{3/2}} = \frac{f(\varepsilon)}{\rho}\left(\frac{\gamma K}{\varepsilon Q}\right)^{1/2} \tag{1.2}$$

Here, ρ is the propellant density, R_{jet} is the jet radius, $f(\varepsilon)$ is a scaling equation, K is the electrical conductivity, ε is the permittivity, and Q is the flow rate. As the flow rate into the jet decreases, the size of the droplets decreases and the charge to mass ratio increases. This means that for smaller droplets, a higher specific impulse can be achieved for the same accelerating voltage application, as shown in Equation 1.3 [9].

$$I_{sp} = \frac{\sqrt{2V(q/m)}}{g} \tag{1.3}$$

Specific impulse is a performance metric that correlates with the exhaust velocity and the

firing time of the thruster. In viewing these equations, it becomes apparent that in order to generate a high specific impulse, very small diameter capillaries must be used to decrease the droplet size and increase the charge to mass ratio. By then applying electrostatics equations in tandem with geometric formulas based on the capillary dimensions, the necessary starting voltage for a capillary of radius R_c can be found in Equation 1.4.

$$V_{start} = \sqrt{\frac{\gamma R_c}{\varepsilon_0}} ln \frac{4d}{R_c} \tag{1.4}$$

The thrust produced by a PIR operating electrospray thruster can further be found in Equation 1.5 [9].

$$T = I_n \sqrt{2 \frac{m}{q} V_{beam}} \tag{1.5}$$

In Equation 1.5, T is the thrust, I_n is the supplied current, m/q is the inverted charge to mass ratio, and V_{beam} is the beam voltage. Though generating a higher charge to mass ratio is beneficial in increasing the specific impulse, it decreases the amount of thrust that the thruster is able to generate, making it useful in long duration spacecraft missions. These equations can be further used to find the thrust to power ratio of the thruster, as well as the thruster efficiency using Equation 1.6 [10].

$$F_W = \frac{F}{P_{in}} = \frac{2\eta_t}{gI_{sp}} \tag{1.6}$$

1.1.3 Purely-ionic Regime

Electrospray propulsion is able to generate thrust through the acceleration of propellant using the application of a voltage source. However, this method of propulsion can create a variety of species from an ionic liquid propellant [11]. Colloid thrusters, for example, generate larger mass droplets from the propellant. This was seen to be ideal originally as the higher mass droplets correlated with a higher thrust [1]. However, to provide sufficient thrust for most missions, these thruster arrays required a large number of emitters with a very large applied

voltage to produce a high specific impulse. Further, these emitters would often operate in the mixed regime, emitting a variety of sizes of species (though monodispersity is possible), causing the efficiency of the thruster to be decreased, because the larger emitted particles will carry higher mass, while the smaller emitted particles and ions will carry higher charge, resulting in a varied species acceleration. The overall efficiency of the electrospray thruster is a product of the ionization (η_i), transmission (η_{tr}), angular (η_θ), and energy (η_E) efficiencies, as well as the polydispersive efficiency (η_P), as shown in Equation 1.7 [3].

$$\eta_T = \eta_i \eta_{tr}^2 \eta_\theta \eta_E \eta_P \tag{1.7}$$

The polydispersive efficiency observed by an electrospray thruster for two species is shown in Equation 1.8, and depends on the variety of species observed within the electrospray plume [3].

$$\eta_P = \frac{[1-(1-\sqrt{\zeta}f_1]^2}{1-(1-\zeta)f_1}\zeta = \frac{(q/m)_2}{(q/m)_1}f_1 = \frac{I_1}{I_1+I_2} \tag{1.8}$$

In this equation, the ζ value refers to the ratio between the charge and mass for two different species within the propellant plume. In order to increase the minimum efficiency, this value must be kept as large as possible, meaning that the species must be as similar in charge to mass ratios as possible. Therefore, to increase the efficiency of the electrospray thruster, it is important that all particles have the same specific charge, which is easily accomplished when all of the particles are monodisperse. This can be accomplished easily when the thruster is operating in the PIR, when all emitted species are ions, and due to their high charge to mass ratios, this also allows for high specific impulses to be achieved at lower applied voltages. The necessity to operate in this regime largely guided the design process of the thruster described in this thesis.

1.2 Electrospray Thruster Challenges

Though electrospray thrusters are a promising form of space propulsion, there are several issues with the current technology that has prevented it from being used largely in space missions. This is due mostly to the sizing and geometry constraints necessary for PIR emission, as well as thruster lifetime due to the monolithic design of the arrays and their lack of material and manufacturing uniformity.

1.2.1 Geometric and Sizing Constraints

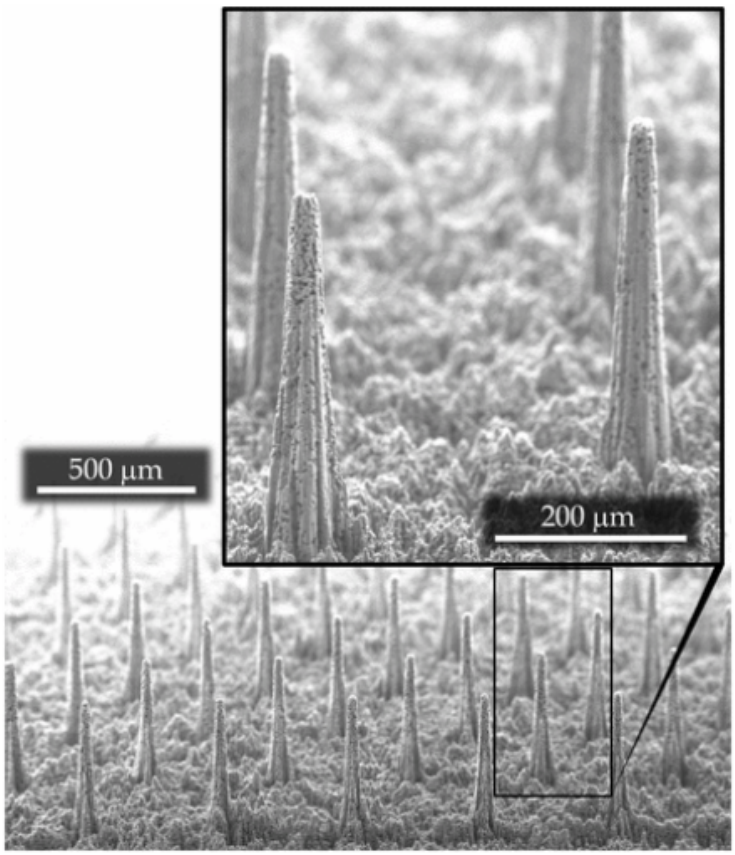

Figure 1.2: Electrospray emitter tips fabricated in carbon xerogel [12]

As described earlier, there is a narrow range of flow rates, currents, and meniscus sizes that will allow for PIR emission, which are influenced by the geometry of the electrodes.

Electrospray thrusters have been recently fabricated as a series of emitter tips on a surface, some of these surfaces being made up of porous materials in order to aid in the passive uptake of propellant to the emitter tip, as shown in Figure 1.2 [12]–[14].

These tips must be made from a material with a pore size that creates sufficient hyrdaulic impedance cause PIR emission to occur, and are built with small, sharp geometries. This causes the emitter tips to be fragile and difficult to manufacture. Further, these geometries must be extremely precise in order to ensure that the meniscus formed at the end of the emitter is axially symmetric and stable, which can be easily affected by small issues in manufacturing and material degradation.

1.2.2 Thruster Shortage and Monolithic Extractor Design

The geometric constraints are not only required for proper thruster operation, but these geometric considerations as well as the operation of the thruster and material selection play a large role in the lifetime of the thrusters [15]. Overall failure of the electrospray system occurs when the extractor fails due to a shortage, but can occur due to several mechanisms.

Backspray is a component that can lead to electrospray thruster failure, in which the propellant begins to spray onto the emitters. This can be caused by overspray, in which too much propellant is sprayed onto the extractor grids, causing extractors to be impinged by propellant, which can cause backstreaming. The geometry of the thrusters, such as extractor misalignment, can also cause secondary electron backstreaming due to ion grid impingement, which could result in a flux of electrons towards the emitter, which can damage the emitter and cause the propellant to decompose [16], [17]

Recently, electrospray thrusters have been constructed as an array of emitter tips in a porous material from which the propellant is emitted. These designs are advantageous in that they allow an easier method of propellant uptake to the emitter site through capillary action. However, these thrusters often have propellant accumulation that occurs on the emitter tip, caused by excessive pooling of the propellant on the emitter profile and around

the emitter, causing shortages and resulting in the lifetime of these arrays to be very short, in some cases less than 200 hours [13]. This pooling occurs randomly, making the lifetime of the thrusters unpredictable, causing their use in space missions to be risky. If any of these mechanisms occur at any single emitter causing the extractor to short, the entire extractor is shorted and cannot continue to fire any of the emitters in the array.

1.3 Micromanufacturing and Porous Substrates

1.3.1 Micromanufacturing

There are several different types of small-scale manufacturing techniques that are used for a variety of applications. The main types of these include [18]:

- Additive manufacturing, in which a desired material is deposited on to a given substrate or medium. Some techniques include digital light projection technology (DLP), lithography, inkjet printing, polymer deposition, and chemical or physical vapor deposition, to name a few [19].

- Subtractive manufacturing, in which a material is removed from a given substrate or medium. Some examples include micro-milling and micromachining using electron beams, abrasive jets, and electrochemical methods.

- Mass containing, in which a material is shaped into a pattern using a form or cast. Some methods of this include extrusion, molding, and forging.

- Joining, in which two pieces of material are bonded to one another, usually through welding, soldering, or chemical bonding.

There are several other processes that are also used to finish micromanufactured structures on the nanoscale, such as grinding or lapping, or using other chemical or abrasive polishing methods. Each method has advantages and disadvantages, and the choice of which method

to use is largely influenced by the scale, material, precision, and geometries required. Additionally, some hybrid machinery have been developed that use both additive and subtractive manufacturing techniques simultaneously, which are particularly advantageous in repairing pieces and creating more precisely manufactured pieces, as the combination of the two methods allows for a higher tolerance to be maintained on the parts manufactured, and can allow for any type of repair to be made, whether material needs to be removed or added [20].

1.3.2 Photolithography

Photolithography is a process by which a photoresist is exposed to a light source of a given wavelength in order to induce a reaction within the photoresist, causing it to cross-link and change its solubility. The light can be applied to specific regions of the photoresist using a directed laser, or through exposing the entire sample with a mask covering portions where exposure is not desired. It is very commonly used in micro-electromechanical systems (MEMS) and semiconductors, and is even used for biological purposes, such as in tissue engineering [21]–[23]. A large goal of photolithography research and development currently is producing smaller minimum feature sizes with increased reliability and high resolution [24], [25].

There are several reaction pathways that can occur during exposure, but all result from the excitation of a ground-state molecule following light irradiation, leading to a photophysical or photochemical transformation [26]. Depending on the chemical used, for most common photolithography uses, this will cause the film to become either soluble in a developer that it was not soluble in prior to light exposure, or become insoluble in a developer that it previously was soluble in. These two resulting patterned films are created using positive or negative photolithography respectively.

There are several advantages and disadvantages to using either positive or negative photolithography. In particular, negative photoresists tend to be softer and lower in resolution, but display better pattern collapse performance than positive photoresists [27]. Though it is

important to note their advantages and disadvantages, often the determination of whether a positive or negative photoresist is used for a certain application depends on the size and structure of the desired features. For example, it often does not make sense to use a positive photoresist if only a few small features need to be formed over a large area, as a positive photoresist would be more suitable for a design that needed a large photoresist structure with smaller features removed from the film.

1.3.3 Porous Substrates

Porous materials have been widely studied for their applications in microfluidics [28]–[31], heat transfer [32], electrodes [33], and vibration control [34] to name a few applications, due to their ability to quickly transport energy and liquids via capillary forces, making them particularly useful in sensor applications that require quick and precise measurements. There have been several methods employed to create porous materials. This includes spark plasma sintering and furnace sintering of metallic and ceramic powders and shells [35], [36], and gas introduction for biopolymers and other biomaterials [37].

A particularly important porous material that is used widely in microfluidics and will be explored in this thesis is porous glass. Porous glass can be manufactured through several methods including direct printing of scaffolds [38] and capillary suspension processing [39] to create pores ranging in size from tens of nanometers to tens of microns. Pore size is very important for ionic liquid electrospray thruster applications, as any potential porous material will need to have pores that are as large as possible without being too large as to interfere with the emitter geometry. For microfluidic applications, these materials often need to be processed in order to build channels on the glass or within the glass to control flow and droplet size [40]. These channels have been processed using methods such as etching, molding, powder blasting [41], [42], and more recently femtosecond laser writing [43], [44].

Though these methods are able to produce small channels and structures accurately within the glass, often there is a necessity for non-porous structures to be built on top of the

porous material. Some methods have been used, such as utilizing lasers or electroless deposition, to deposit various metals onto porous silicon wafers [45]–[47]. However, these deposition methods were not able to create well-defined, high-resolution geometries on the substrate surface, and little literature exists describing deposition of materials onto porous glass substrates. SU-8 electron beam lithography has been completed on solid glass substrates, not porous glass, through the use of hexamethyldisilazane (HMDS) to promote adhesion between the SU-8 and glass since SU-8 does not adhere well to glass alone [48]. An important note in Vinje et al. is that by spacing thicker portions of cross-linked SU-8 closer together, there begins to be partial undesired cross-linking in areas between the SU-8 patterned regions. This will be very important in this thesis, as it is important that small areas between large areas of cross-linked SU-8 are properly resolved and do not become cross-linked so that the capillaries may remain clear and open to propellant uptake.

1.3.4 Volatile Organic Compounds

VOCs are characterized by their high vapor pressure and low water solubility. They are used in several household products from gasoline and fuels, to personal care products and cleaners, as well as in industrial manufacturing settings. VOCs can vary largely in their boiling and melting points, as well as their vapor pressures [49]. Though these compounds can be very versatile and advantageous to use, it is important to note their hazards and environmental impact. Due to their properties, VOCs can easily enter the environment, making most research into them focus on how to contain them and reduce their environmental impact. VOCs are generally highly toxic and some are carcinogenic, such as benzene, and are harmful to both the ecosystem and environment. Several containment systems are used to keep VOC environmental emission to a minimum, including adsorption, condensation, and oxidation methods [50]. Though they are generally harmful, they will be key in this thesis, as their high vapor pressure and low boiling points will allow for easy melting and later sublimation within porous glass substrates.

1.4 Thesis Contributions

This thesis aims to work towards understanding the lifetime and geometry issues associated with electrospray thrusters, and propose a new electrospray thruster design and fabrication process using the above mentioned manufacturing techniques to reduce these issues. The design and its manufacturing process, which will be explored in later sections, generally consisted of two key design components.

First, the currently-used emitter tip design was replaced instead with a capillary design, to allow for precise geometric control over the meniscus size and pinning. This was completed through the use of photolithography to create high resolution micron-scale structures on top of a porous substrate. To prevent the photoresist from entering the pores during fabrication, the porous substrate was loaded with a VOC that was solid at room temperature but could be easily melted to saturate the pores with it, and later sublimated to remove it from the pores post-processing.

Second, the capillary emitters were constructed with individualized, integrated extractors, that were built on top of a layer of photoresist around the emitters. These extractors were constructed as conductive rings around each extractor, and connected to one another through a series of fuses, sized so that they would fuse at a current in the range of currents experienced by extractors during a thruster shortage. Upon contact with a current from a shortage, the fuses would disintegrate, preventing the shortage from propagating to the rest of the extractors, allowing the rest of the array to continue to fire.

The design would allow for a greatly increased thruster lifetime and efficiency. Referred to as "pixel" thrusters, each individual emitter in the array would function like a pixel in an LED screen, where if a single pixel stops functioning, the rest of the screen is able to still produce an image. In other words, the shortage of a single emitter would not result in the full shortage of the extractor, and the rest of the array would be able to continue firing in the case of a single emitter shortage. Further, through photolithography techniques allowing for

high resolution capillary fabrication, these emitters can be more consistently manufactured in the correct dimensions to operate in the PIR and centered properly within the extractor, allowing for more efficient and reliable thruster operation. This thesis focuses on the design and manufacturing processes required to build this design, and later testing will be necessary to verify its ability to produce PIR emission and other performance metrics.

Chapter 2

Manufacturing Constraints and Thruster Design

In order to design the thruster, the geometry and materials chosen for the thruster must be consistent with the dimensions required for both fuse functionality and electrospray thruster firing. This section will detail the requirements for the sizing and materials used for the thruster. The overall design will resemble the designs shown in Figures 2.1 and 2.2.

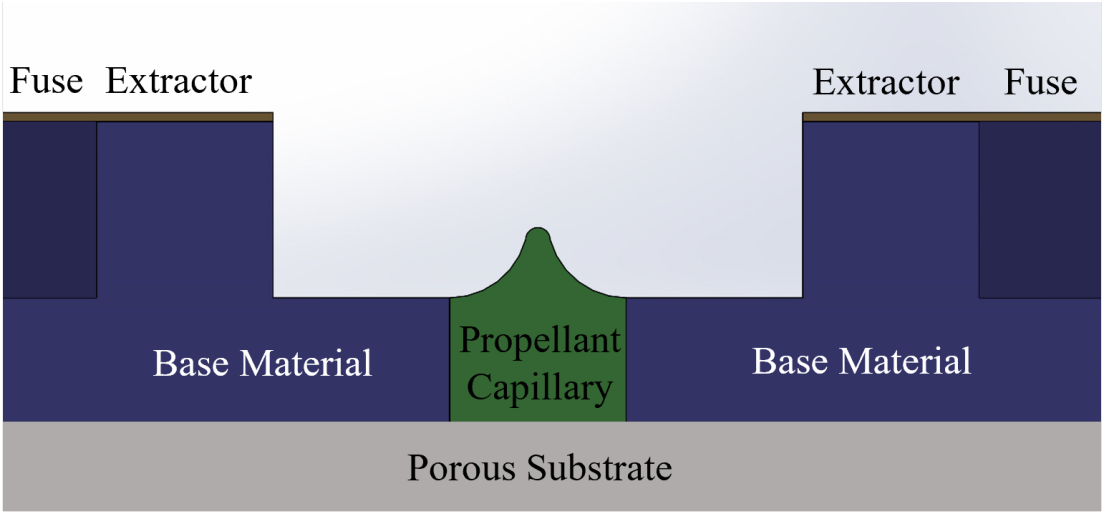

Figure 2.1: Single Emitter CAD Preliminary Design

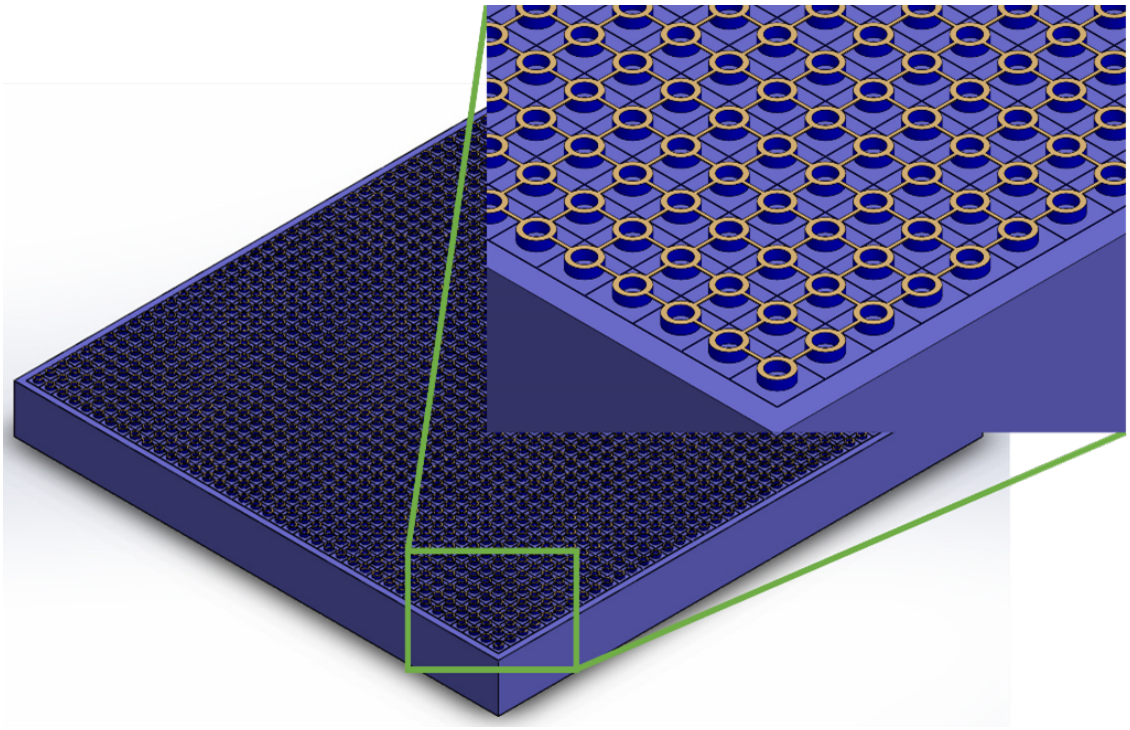

Figure 2.2: Full Array CAD Preliminary Design

2.1 Size Constraints

2.1.1 Emitter Capillary

In order for the thruster to be able to properly operate within the PIR, the emitter must have specific dimensions. To produce a stable electrospray plume while maximizing current, the capillary must have an impedance that surpasses the PIR impedance. The impedance for producing PIR thrust, Z_{PIR}, for common propellant sources in electrospray thrusters is in the order of 10^{17} Pa/m^{3}s for EMI-BF_4 [51]. To ensure that the impedance remains in this range, without being excessively large as to significantly decrease the emitted current, the impedance of the capillary should be approximately 2-3 times Z_{PIR}. However, because the emitters will be built on a porous substrate, the impedance generated by the porous substrate can account for part of the necessary impedance to reach Z_{PIR}. This can be found using Darcy's law, which uses the permeability of the porous media to determine the impedance

as shown in Equation 2.2 [52]. The permeability of a porous media can be derived from the Kozeny–Carman equation, assuming that the pores are spherical and of constant size, as shown in Equation 2.1 [53].

$$k = \frac{\epsilon^3 d_p^2}{180(1-\epsilon)^2} \tag{2.1}$$

$$Z_s = \frac{\mu L_s}{kA} \tag{2.2}$$

In Equations 2.1 and 2.2, k is the permeability of the porous substrate, ϵ is the void percentage of the porous media, and d_p is the average pore diameter, Z_s refers to the substrate impedance, μ is the liquid viscosity, L_s is the substrate length, and A is the cross sectional area of the substrate. The impedance generated by the capillary (Z_c) can be determined using the Hagen-Poisseuile equation, shown in Equation 2.3.

$$Z_c = \frac{8\mu L_c}{\pi R_c^4} \tag{2.3}$$

L_c refers to the length of the capillary and R_c refers to its radius, which will be equal to the meniscus radius formed from which ions are emitted, and µ refers to the viscosity of the liquid. The total impedance generated by the capillary-substrate system, Z_t, can be found in Equation 2.4.

$$Z_t = Z_s + Z_c \tag{2.4}$$

Knowing that Z_t must be at least 2-3 times Z_{PIR}, and using parameters for the permeability of the porous substrate assuming a material similar to Corning's porous Vycor 7930 of a size identical to the substrates currently used in the Space Propulsion Lab (10 mm square, 1 mm thick chips), the length and radius of the capillaries can be related as shown in Figure 2.3.

This R_c value should lie in the range of 1-5 µm, as this is the general stability range for $R_{meniscus}$ [54]. Additionally, this radius size would ensure that the propellant does not clog up the emitter, as sizes below this have often resulted in a failed firings due to propellant

clogging [55]. Using this constraint, L_c should be approximately 2-30 µm depending on the R_c selected. These values will need to be more thoroughly calculated for different propellant sources, but this will serve as a starting point.

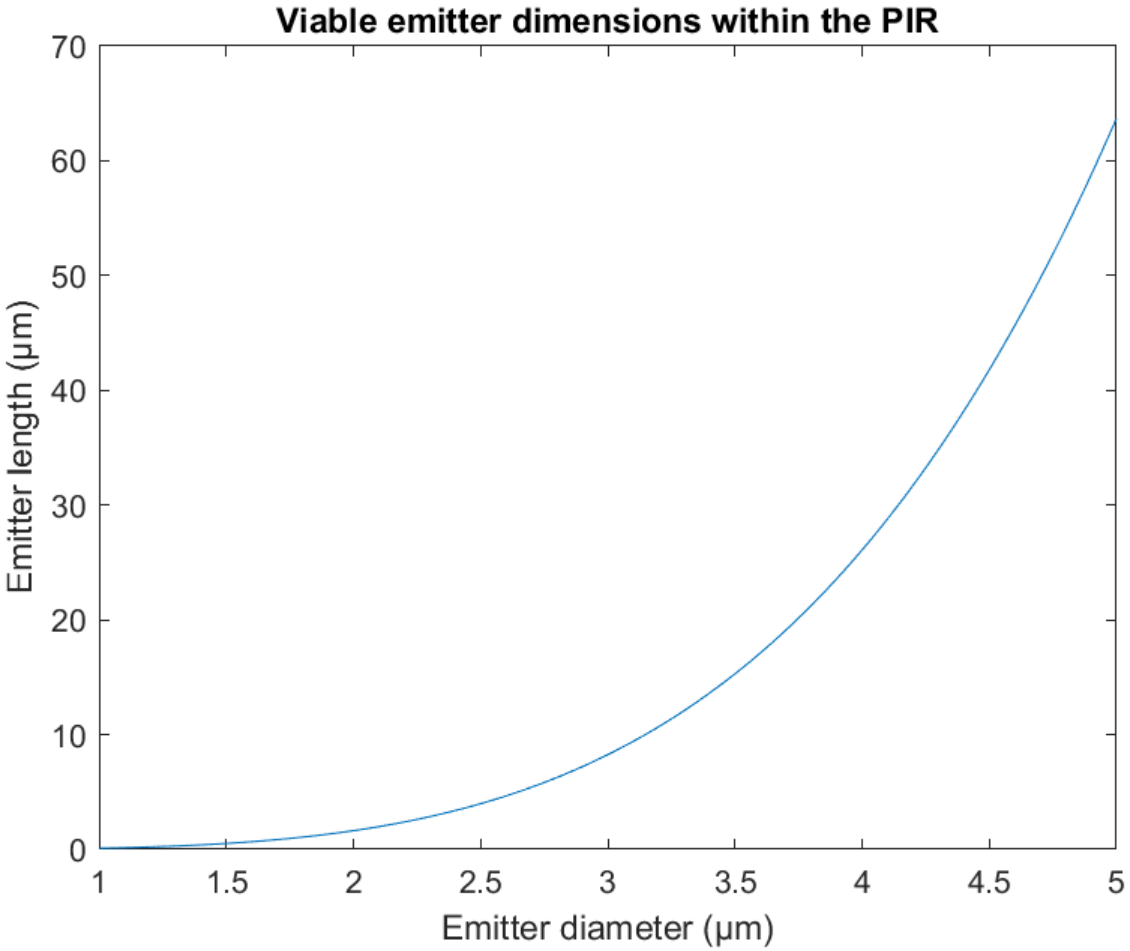

Figure 2.3: Emitter diameter vs. length plot based on Equations 2.3 and 2.4, using EMI-BF_4 at room temperature.

2.1.2 Fuse

The fuses connecting the extractors will need to be properly dimensioned to ensure that the change in current caused by an emitter shortage will result in the fuse's disintegration. Disintegration of wires with circular cross-sections via fusing is governed by the fusing equation

found by Preece in Equation 2.5 [56].

$$d = (\frac{C}{a})^{\frac{2}{3}} \tag{2.5}$$

In the equation, d represents the wire diameter, C represents the current, and a is a constant found for the fusing material used. For gold, this constant is noted as 10,244 $A/m^{3/2}$. Assuming a fusing current of 1 mA, this would require a fuse diameter of 21.2 µm, which is feasible though relatively large in comparison to the desired scale of the emitter/extractor configuration. This equation lacks in that it does not account for a rectangular cross section that will likely be used. Further, when initially testing the fuses in atmosphere, convection will play a role in the cooling of the fuse and therefore the fusing current, which is not taken into account in Preece's equation, though this may not be an issue during in-vacuum testing. Additionally, to create free-hanging fuses that are capable of fusing at a low current of approximately 1 mA would be too difficult, as manufacturing techniques would likely not allow these bridges to be properly manufactured and remain intact throughout the fabrication process. Therefore, the fuses will likely need to be built on top of supports to ensure they remain intact until fusing occurs. This adds conduction between the fusing material and the material supporting it as a major factor in the fusing current required, and therefore to determine the best fuse material and sizing, a COMSOL Multiphysics simulation using the Joule Heating module will be used instead of traditional fusing formulae.

2.2 Material Constraints

2.2.1 Thruster Base

Using these values, different materials and machining methods can be examined for their use as the array panel material and means of manufacturing the required geometry. The concept of creating a PIR electrospray thruster on a flat surface has been supported by

analytical and experimental studies [57]. This is because the liquid column created using the capillary structure can mimic the role of the sharp-tip geometry used in conventional electrospray thrusters. This is on the condition though that the material used has a low dielectric constant, as these materials will require the least amount of voltage to produce the necessary differential to produce PIR thrust [57]. One example of these materials is polydimethylsiloxane (PDMS), which is a common dielectric used in micro/nanofabrication that can be fabricated at resolutions similar to the requirements for this design. Another option for this also includes SU-8, which likewise has a low dielectric constant and can be micro/nanofabricated easily, and made durable using a hard-bake step post-processing. Several studies have recently been completed using SU-8 as well to create capillary electrospray thrusters, also making it likely a good candidate material [58]–[61].

Though low dielectric constant materials will be ideal, there is the potential for collisions or instabilities within the plume to result in the deposition of charged ions onto the oppositely charged dielectric. This can affect the electrostatic boundary conditions of the system, and therefore the stability and efficiency of the thrust plume and operational voltages. Later simulations will need to be completed to better understand these effects and choose materials that can still produce efficient emitters if this proves to be an issue.

These materials will also need to be easily machinable and processable in batches to ease in scalability to larger surfaces. Photolithography is a potential candidate for machining these small holes with these geometries, which may be able to create the necessary geometry needed to create cuts in SU-8 as small as 24 nm, as shown in a 2006 study [62]. PDMS has also been layered into precise geometries using SU-8 and masking techniques to create pillars as small as 1.5-2 µm [63]. There are a variety of photolithography resources with similar precision that are available at MIT: MIT.nano photolithography facilities can be used to spin coat and cut SU-8 in dimensions sufficient for the size constraints of the design.

2.2.2 Porous Substrate

These materials will need to be manufactured on a porous substrate. Porous materials have been used as the base for electrospray thrusters, as their porous structure allows for passive propellant uptake from a propellant reservoir into the emitter region of the device [12]. However, it is desirable to use materials that can be manufactured using the photolithography techniques available in the MIT.nano facilities. This means that the substrate needs to be able to have a material spun on top of it, without allowing the emitter structure material to penetrate into the pores. Otherwise, the pores will become clogged and no propellant will be able to uptake into the emitters. To avoid this, the porous substrate will need to be saturated with a volatile organic compound (VOC), that can be sublimated to allow a thin layer of the glass to be exposed to the surface so the manufactured emitter capillaries can stick to the glass surface, and then be completely removed through melting or sublimation after the array has been manufactured on the surface. There are several options for this material, including fluorene and anthracene, that have moderate melting points to allow for easy melting and removal from the glass, as well as low vapor pressures to allow for easy sublimation [49], [64].

2.2.3 Extractor and Fuse

An elevated photoresist structure consisting of rings connected by fuse bridges will need to be manufactured, and these ring and fuse regions will need to be coated by a conductive material, serving as the extractor regions and fuses respectively. A material that is durable, conductive, and can be easily applied to a surface in precise regions is required, such as gold. Gold can be deposited easily via sputtering, making it a good candidate. However, gold has a very low electrical resistance, making it a poor candidate for a fuse that can function as the desired currents. Therefore, other metals with higher resistance will be looked into that can also be deposited through sputter coating, such as a nickel-chromium alloy and

tin. To deposit the metal in precisely patterned regions to form the extractors and fuses, several methods can be employed ranging from using a sacrificial SU-8 layer to using positive photoresist masking and liftoff to produce the desired metal patterns. These will be tested, and the best patterning option will be chosen based off experimentation.

Chapter 3

Manufacturing

3.1 PDMS Thruster Design

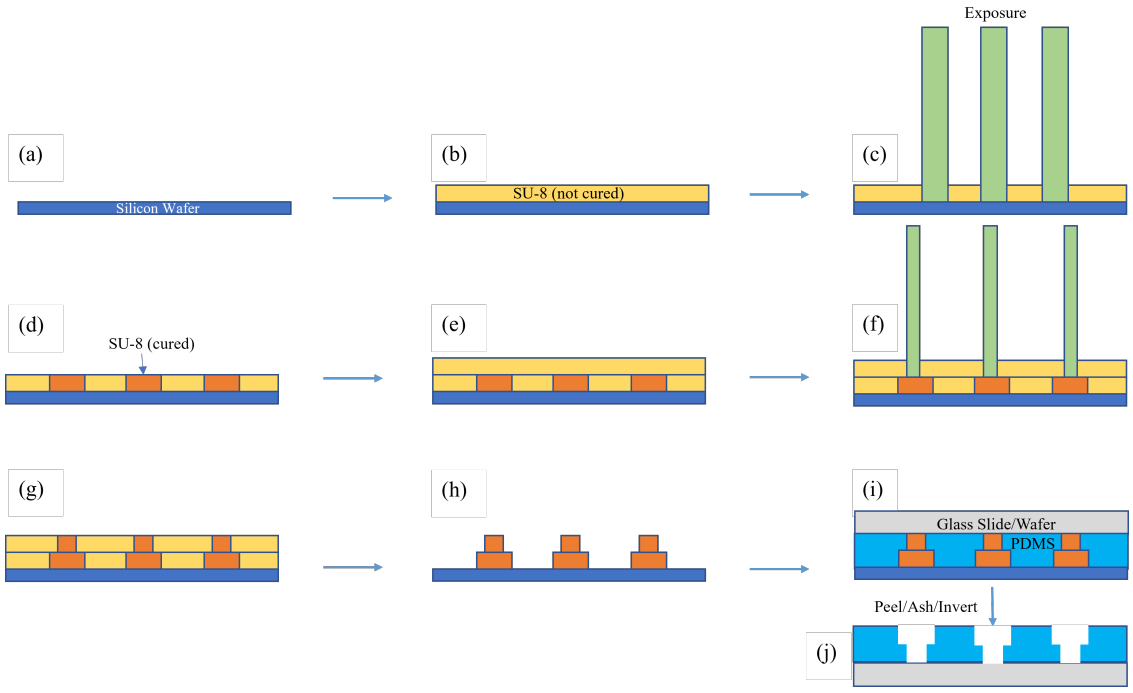

Figure 3.1: SU-8 mold and PDMS thruster design process.

To build the emitter and extractor base, a process was first attempted that involved making an SU-8 mold that PDMS was then poured over to create the desired geometries. In this design, a silicon wafer substrate (3.1 (a)) was initially spun with a layer of SU-8 and

post-spin baked (3.1 (b)), then it was exposed with a 375 nm DirectWrite MLA maskless aligner laser in the desired pattern inverse of the extractor region (3.1 (c)). The substrate was then soft-baked to fully finish the cure process of the SU-8 (3.1 (d)). Next, the substrate was spun with a second layer of SU-8 and post-spin baked (3.1 (e)), exposed again with the MLA in a pattern inverse to the emitter region (3.1 (f)), and soft-baked once more (3.1 (g)). The entire substrate was then developed in propylene glycol monomethyl ether acetate (PGMEA) to remove uncured SU-8 (3.1 (h)). The development process involves placing the substrate in a pool of solvent that either only the exposed or only the unexposed regions are soluble in, depending on if positive or negative photolithography was used, effectively patterning the layer. SU-8 is a negative photoresist, and therefore exposed regions became insoluble to the developer, allowing the unexposed regions to dissolve when developed. Next, a pool of PDMS was placed on top of the SU-8 mold, and a glass slide was pressed against it until it cured (3.1 (h)). Once the PDMS cured, the glass slide was peeled from the SU-8 mold and inverted to reveal the emitter and extractor design (3.1 (i)).

Initially thought to be the best material option due to its flexibility and low dielectric constant value, PDMS was first chosen as the material to use for the thruster emitters. In order to create the emitters out of PDMS, a mold was first constructed using SU-8. The PDMS was then poured over top of the SU-8 mold, allowed to cure for 24 hr, and peeled off to create the thruster geometry. The process diagram in Figure 3.1 shows the SU-8 mold fabrication process followed by PDMS demolding. Each layer of SU-8 shown in the graphic is approximately 8 µm in thickness, with the exposure areas varying in width from 3 to 21 µm.

SU-8 2005 was utilized to create the desired thickness for the extractor and emitter layers. First, the proper spin and exposure parameters, including spin speed and exposure dosage, were found for the SU-8 2005 material used. The spin speed versus SU-8 thickness is shown in Figure 3.2. The thickness was read at various spin speeds using a Dektak150 profilometer.

It was found that a spin speed of 1050 rpm could be used to create 8 µm SU-8 layers, which would correspond well with generating PIR impedance for 3 µm emitter capillaries

in Equation 2.3. For simplicity, the depth of both the emitter capillary and the extractor height were the same for initial testing. To determine the best exposure parameters, SU-8 was exposed using a DirectWrite MLA, which is a maskless laser used to pattern exposures onto photoresists, with several circles of various diameters. These structures and patterns were designed using Klayout, which is a software that allows for the design of maskless exposure patterns. The best exposure dosage using the 375 nm laser from the MLA was found to be 2500 mJ/cm^2 in order to produce a viable pattern, much higher than the recommended dosage that the manufacturer of the SU-8 2005 solution recommended for this film thickness.

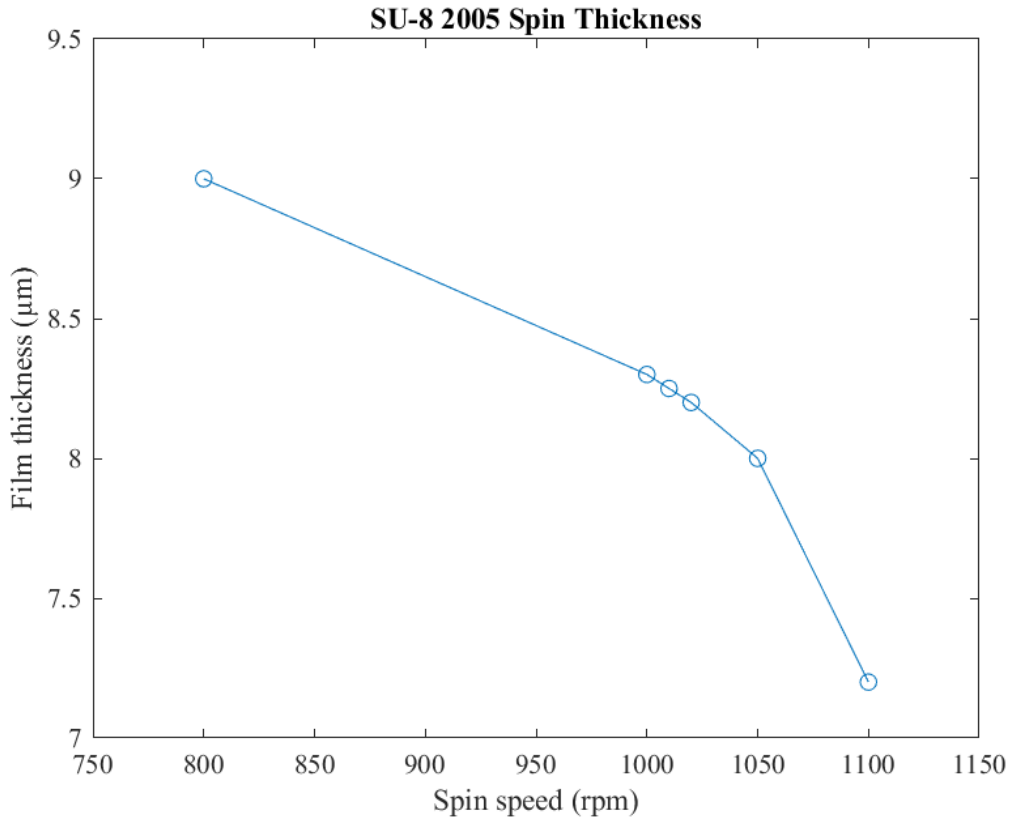

Figure 3.2: Spin speed vs SU-8 2005 material thickness on silicon wafers.

Next, the desired SU-8 molds were fabricated and PDMS was poured over top in order to create the PDMS thruster design. The minimum emitter resolution was found by creating arrays of various geometries in order to find the minimum size that would allow for complete

design transfer. In Figure 3.3, the scanning electron microscope (SEM) images show the PDMS thrusters with emitter diameters as 3, 4, and 5 µm from left to right.

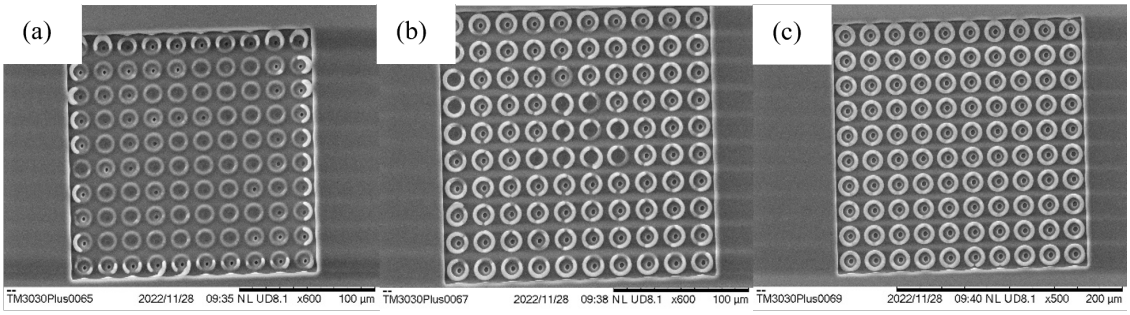

Figure 3.3: SEM Images of PDMS demolded thruster with minimum dimension sizes of (a) 3 µm, (b) 4 µm, and (c) 5 µm.

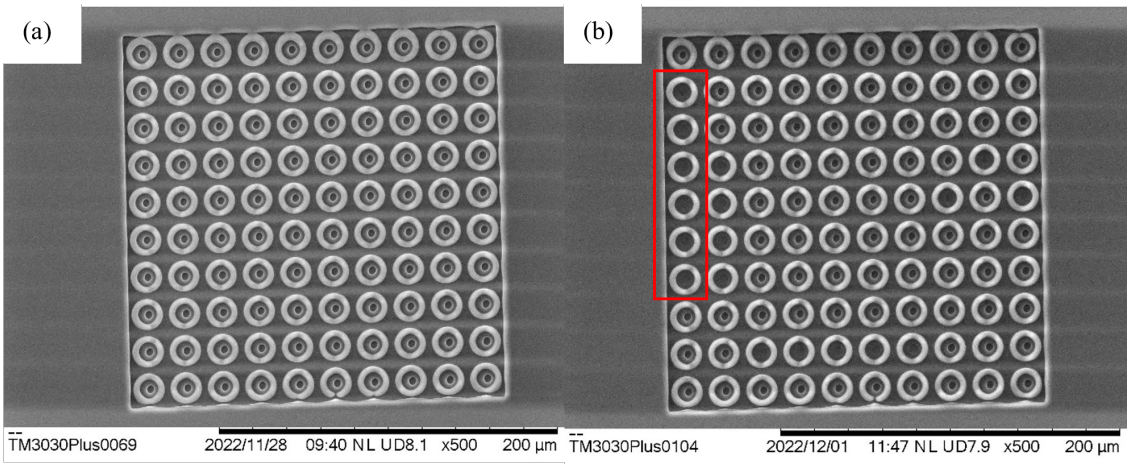

Figure 3.4: (a) First and (b) second PDMS pour and demold from same SU-8 mold, with a red outline indicating emitters that were not properly transferred.

As shown, a minimum size of 5 µm for the emitter capillary diameter was required for complete design transfer from the SU-8 mold to the PDMS. Further, successive PDMS demoldings using the same SU-8 mold showed that an SU-8 mold could only be used once at this scale before damage would occur that would result in successive PDMS demolds losing their desired structure, as shown by some of the extractors lacking emitters in Figure 3.4.

Last, in order to determine the viability of the removal of the remaining PDMS within the emitter capillary region, as this region would need to be clean of PDMS in order to allow propellant to flow up the emitter, profilometry scans were taken of the PDMS thruster

topology in comparison to the height of the glass slide. The profilometry image is shown in Figure 3.5, and due to the large amount of material present in the emitter capillaries, it was determined that removal of the PDMS from the capillaries without damaging the surrounding structures was not feasible.

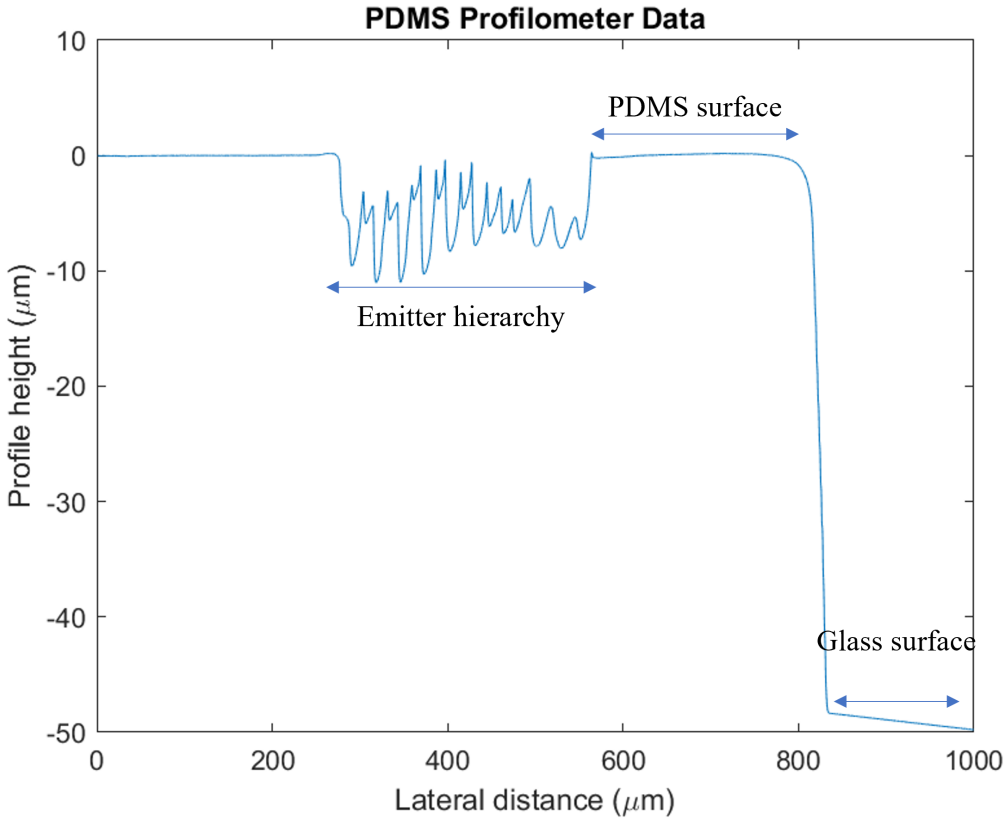

Figure 3.5: Profilometry scan of PDMS thruster on glass slide.

Attempts were made to reduce the residual PDMS thickness beneath the emitter capillaries through adhering the glass wafer to the SU-8 molded silicon wafer, applying high constant pressure as the PDMS cured, and allowing the sample to sit in a desiccator while curing to remove bubbles. Though this reduced the amount of material within the emitter capillary, it did not remove enough to make it feasible to remove the rest using an asher or other equipment, as shown in Figure 3.6.

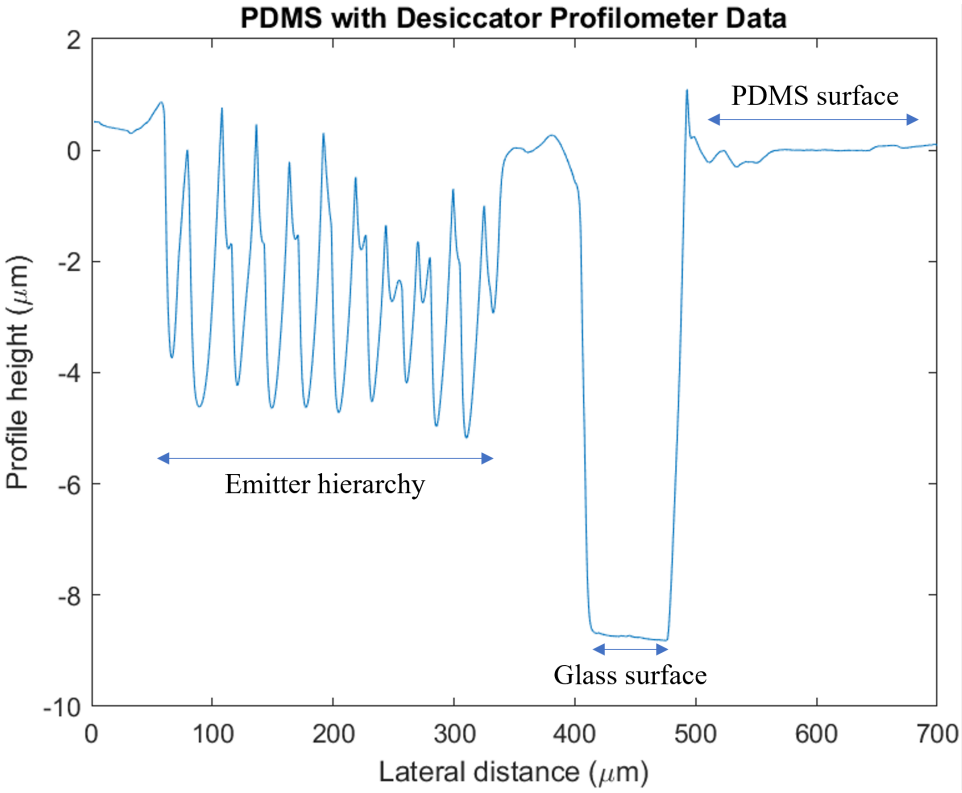

Figure 3.6: Profilometry scan of PDMS thruster on glass slide, cured with desiccator and pressure.

3.2 SU-8 Thruster Design Wetting Tests

Though PDMS was intially proposed as the best material option for the emitters and extractor base, SU-8 is an easily manufactured material that also has a low dielectric constant value of approximately 3, making it a viable candidate for the thruster emitter material. However, it was uncertain as to how wettable the surface of the SU-8 was. For the thruster design, it is optimal that the emitter material is hydrophilic so that it may draw up the propellant, but be able to have a hydrophobic layer added on top to prevent the propellant from pooling and drawing up towards the extractor regions. First, a hard- and soft-baked SU-8 layer was deposited on a silicon wafer and the propellant contact angle (CA) was measured. Next, an approximately 20 nm layer of PTFE was sputter coated onto the SU-8 layers and the CA was obtained again. The droplet images are shown in Figure 3.7.

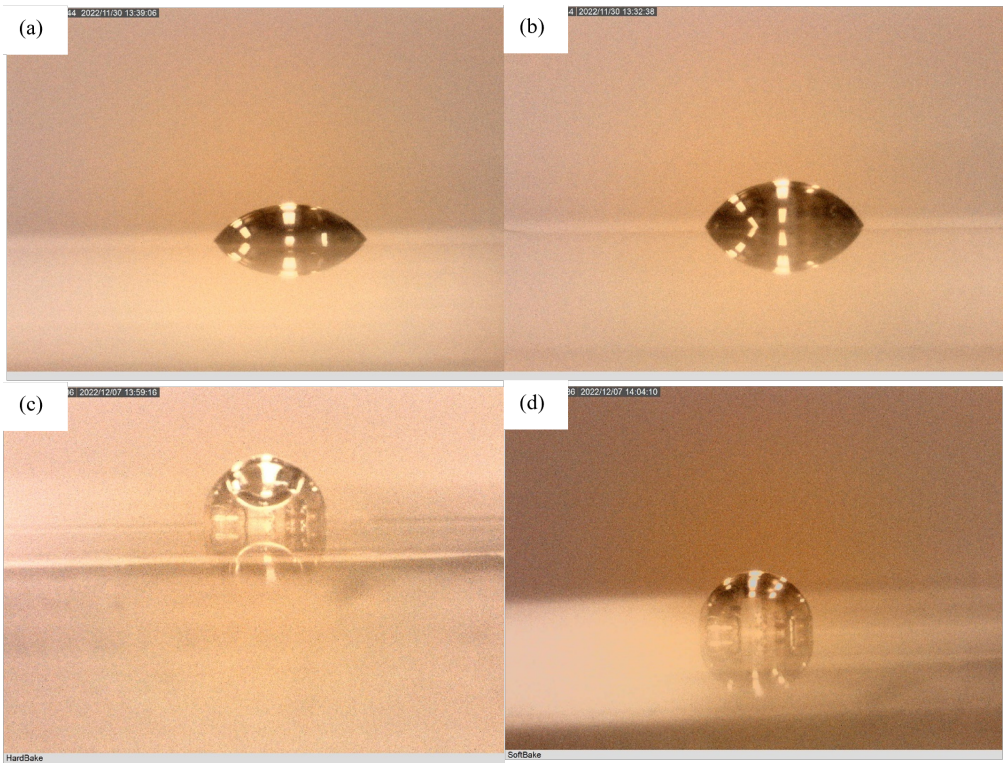

Figure 3.7: EMI-BF_4 2.5 L droplet on (a) hard-baked SU-8, (b) soft-baked SU-8, (c) hard-baked SU-8 with 20 nm PTFE coating, and (d) soft-baked SU-8 with 20 nm PTFE coating.

The droplets consisted of EMI-BF_4. The droplet images were captured using a DinoCam camera and analyzed using ImageJ to determine the approximate CA. In Figure 3.7 (a) and (b), the CA was approximately 70°, while in (c) and (d) it was approximately 90°, meaning that the surface was hydrophilic but could be made hydrophobic through PTFE sputtering, which is ideal. Further, this shows that baking the SU-8 did not significantly impact its surface properties in terms of hydrophobicity or its ability to allow PTFE to adhere to the surface.

Finally, to ensure the propellant would wet the capillary, a series of channels with varying widths to mimic the possible emitter diameter sizes were embedded into a layer of 8 µm thick SU-8, and a droplet of propellant was placed at one end of the channel, and allowed to flow along it. In the 10 to 20 µm range, EMI-Im propellant was able to flow through the entire channel without outside intervention and create a meniscus that pinned at the rim of the channel. However, above this width, though the propellant would attach to the edges of

the channel and flow through the channel, a meniscus would not form across the end of the channel, as shown in Figure 3.8. Because the emitters will likely be under 10 µm in diameter, this wetting behavior should be favorable for the design.

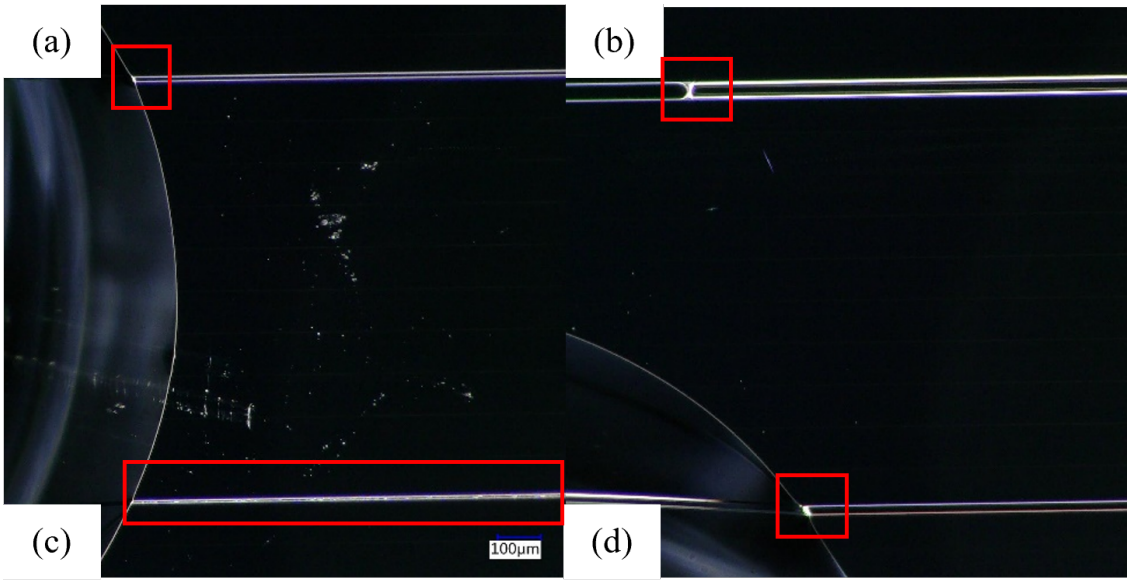

Figure 3.8: Channel wetting of (a) 10 µm, (b) 40 µm, (c) 5 µm, and (d) 20 µm width SU-8 with EMI-Im, with red boxes indicating wetting and/or pinning points

Due to these wetting results, SU-8 was determined to be a viable thruster material option. In order to create the desired SU-8 thrusters, a new process as shown in Figure 3.9 was used. To create the thruster structures, the same method as detailed above to create the SU-8 molds was used. However, an inverted geometry was used so that the thruster design itself would be printed as SU-8 rather than a mold structure. In doing so, the design was able to have a much smaller minimum dimension size and still remain structurally intact, with a minimum emitter capillary diameter of 3 µm achieved.

In this process, the steps in Figure 3.9 (a-h) are identical to those in Figure 3.1, with the only change being the exposure patterns used. In Figure 3.1, the exposure pattern in (c) was the inverse of the extractor shape and (f) was the inverse of the emitter shape. For Figure 3.9, (c) instead involved exposing the exact shape of the emitter, and (f) involved exposing the exact shape of the extractor.

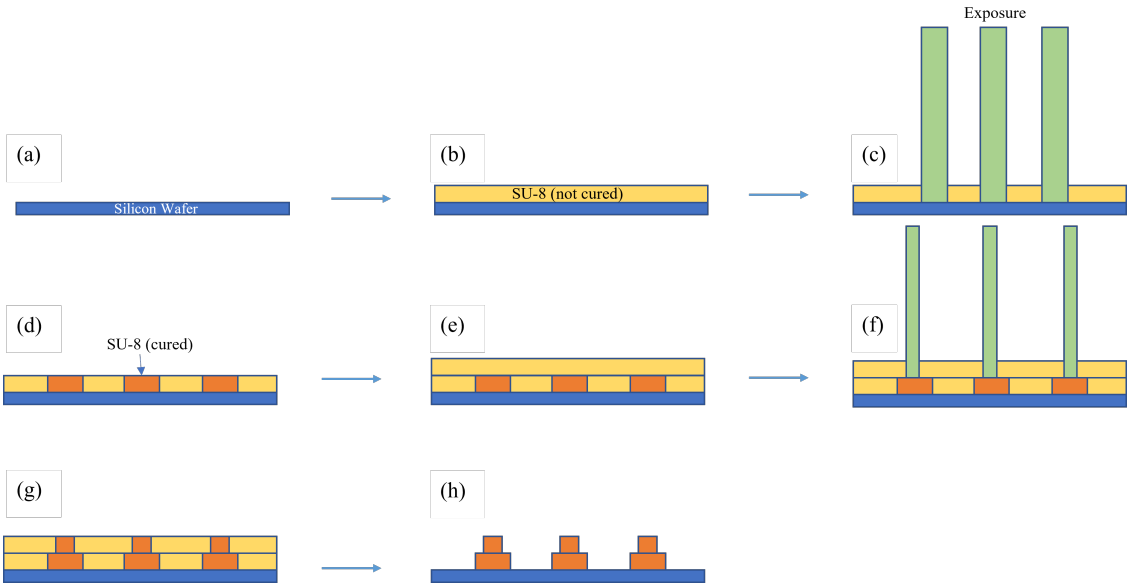

Figure 3.9: SU-8 thruster design process.

3.3 Gold Deposition

To create the extractor and fuse regions in the thrusters, a physical mask could be used to deposit the gold in specific desired regions. However, physical masks are expensive and several would need to be made as the design and scaling of the thruster arrays were consistently being changed during the design process. Therefore, three options were attempted in order to deposit the gold. The first option involved depositing the gold onto the SU-8 prior to development, and then allowing the developer to remove gold from undesired regions by removing the SU-8 beneath it. The second option involved depositing excess SU-8 onto the regions around the extractors and fuses, sputtering gold onto the sample, then using a diamond lapping disc to shave the gold from the elevated SU-8 regions, and then developing the sample to remove the excess SU-8. Finally, the third option was lift-off, which involved depositing a layer of positive photoresist on the SU-8 thruster, then exposing and developing the extractor and fuse regions, sputtering gold, then removing the remaining unexposed photoresist with a solvent.

3.3.1 Sacrificial SU-8 Attempt

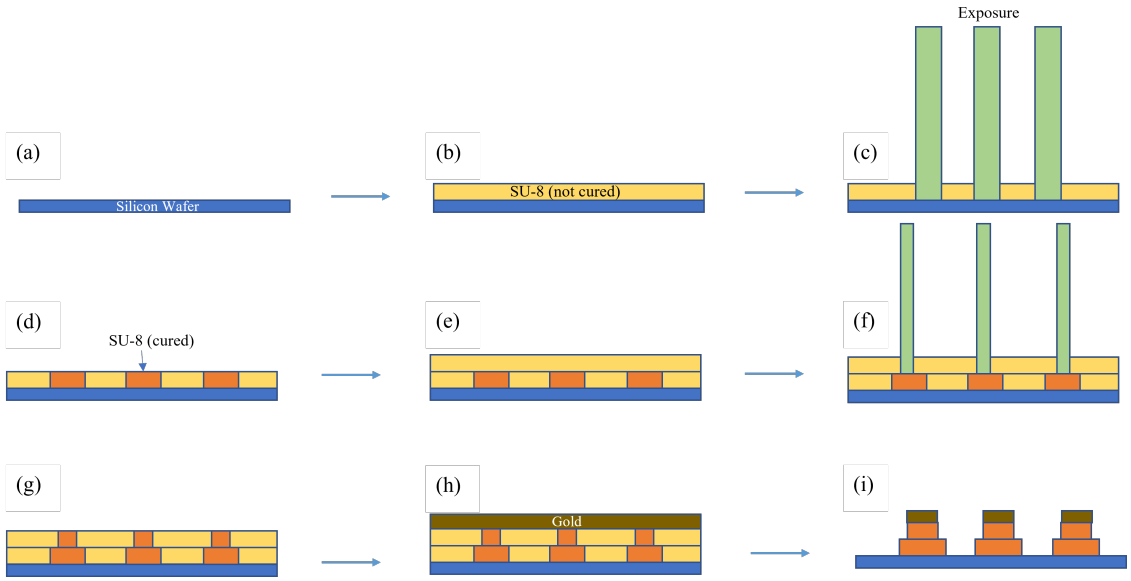

Figure 3.10: Initial gold deposition process on SU-8 thruster.

The first process attempt is displayed in the diagram in Figure 3.10. Steps (a-g) were identical to steps (a-g) in Figure 3.9, however prior to developing the SU-8 in the process in Figure 3.10, a layer of gold was sputtered on (h) and then the sample was developed (i). The gold was deposited using a Sputter Balzer machine and 10 nm of gold was deposited. Upon development, however, regions with gold deposited did not develop, making this method unfeasible. This was possibly due to the plasma depositing the gold causing the unexposed regions of SU-8 to cross-link and prevent them from being soluble in the developer. It is also possible that the gold on the surface prevented the developer from reaching and removing the SU-8 beneath it.

3.3.2 Diamond Lapping Attempt

Figure 3.11 displays the second process attempted for depositing gold on the SU-8 thruster. This method varied relatively significantly from the previous processes. First, the silicon wafer (3.11 (a)) was spun with SU-8 (3.11 (b)) and was then exposed in the emitter regions

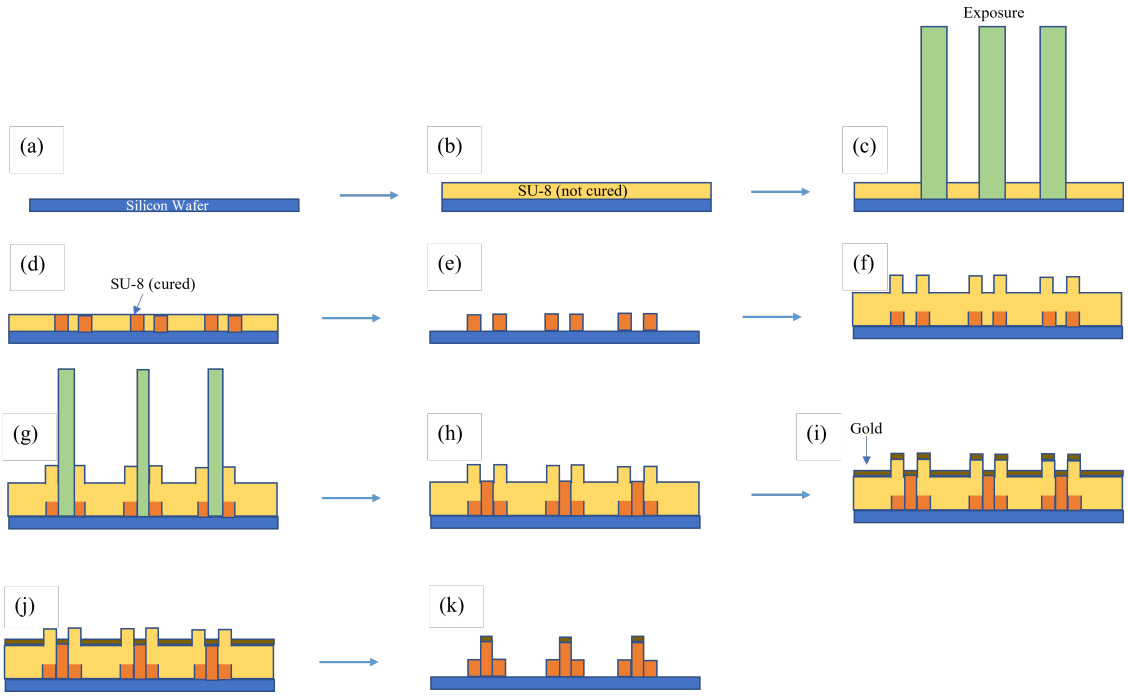

Figure 3.11: Diamond lapping method of gold deposition on SU-8.

only, excluding the regions where the emitter and extractor areas overlap (3.11 (c)). This was done so that after the sample was post-exposure baked (3.11 (d)) and developed (3.11 (e)), when a new layer of SU-8 was spun on top of it (3.11 (f)), the full SU-8 film was thicker in the emitter regions. Following the exposure of the extractor regions (3.11 (g), the only fully exposed SU-8 regions that were at the surface were the extractor regions (3.11 (h)). The sample was then sputtered with a layer of gold (3.11 (i)), and gently sanded with a diamond lapping disc (3.11 (j)) to remove the gold from the elevated SU-8 regions, exposing the surface of these unexposed SU-8 regions to the surface so that they would be more easily developed, removing the unexposed SU-8 and the gold that was deposited on top of it (3.11 (k)).

This method allowed for the removal of the majority of the gold from the unwanted regions, however it caused debris to accumulate within the array structures, destroying the geometry necessary for the thruster design. This is shown in the SEM images in Figure 3.12.

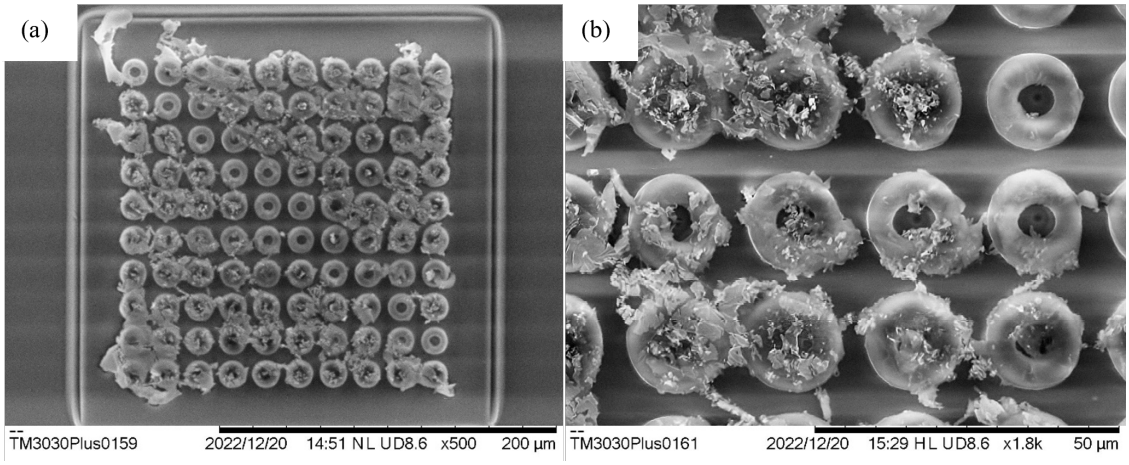

Figure 3.12: SEM images of 3 µm emitter capillary array design post diamond lapping method attempt at (a) 500x and (b) 1800x magnification.

3.3.3 XT10 Photoresist Lift-off Attempt

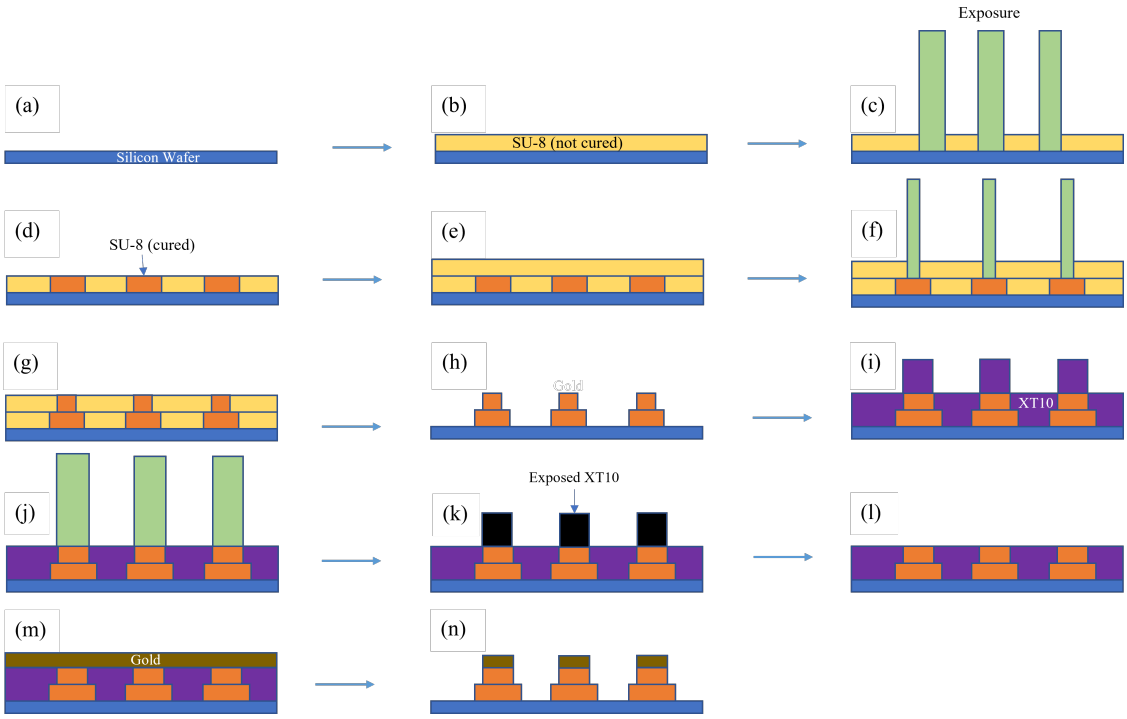

Figure 3.13: Gold deposition on SU-8 using XT10 photoresist lift-off method.

The last method attempted was the utilization of a positive photoresist to serve as a lift-off mask over the SU-8 thruster. The process is detailed in the process diagram in Figure 3.13.

This deposition involved first creating the SU-8 thruster structures in steps 3.13 (a-h) identical to the steps in Figure 3.9 (a-h), followed by spinning a 7.5 µm layer of AZ 10XT (XT10) photoresist onto the surface, post-spin baking and post-bake rehydration (3.13 (i)). The layer was then exposed (3.13 (j), (k)) and developed (3.13 (l)) to leave only the extractor surface exposed to the air. Next, gold was sputtered on the surface (3.13 (m)) and finally an acetone wash and 10 min acetone sonic bath was completed to remove the remaining XT10 and any gold that had been sputtered onto it (3.13 (n)).

The deposition was completed on a variety of array sizes with emitter capillaries ranging from 3 to 10 µm in diameter, with surrounding structures having radii 3 µm larger than the emitter capillaries within them. The deposition was first attempted on a clean silicon wafer without the SU-8 structures, as shown in Figure 3.14. The deposition was then attempted on an SU-8 emitter array, and the resulting microscope images are shown in Figure 3.15.

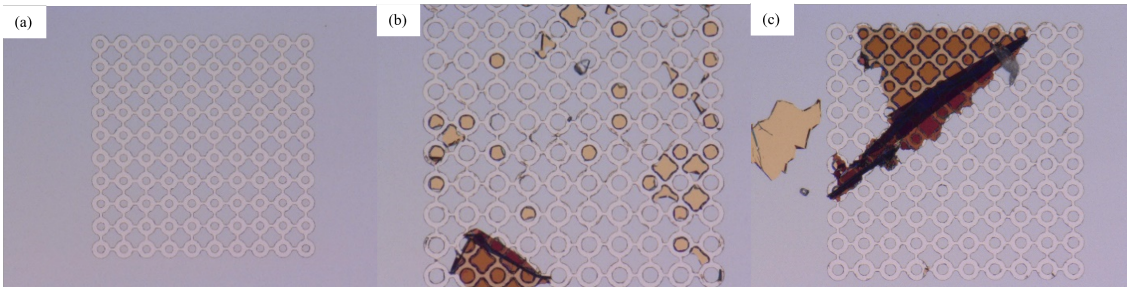

Figure 3.14: XT10 positive photoresist mask pattern of gold on silicon wafer at 1000x magnification with (a) 3, (b) 6, and (c) 10 µm diameter emitter capillary geometries.

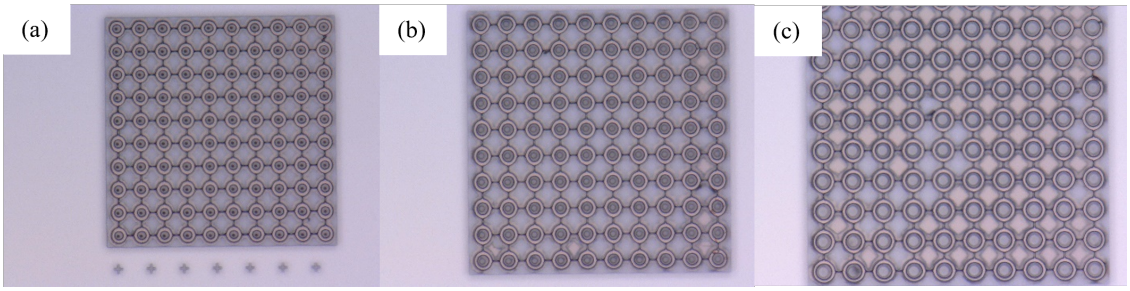

Figure 3.15: XT10 positive photoresist mask pattern of gold on SU-8 thruster arrays on a silicon wafer at 1000x magnification with (a) 3, (b) 6, and (c) 10 µm diameter emitter capillary geometries.

As imaged in Figure 3.14, the larger the scaling of the thruster array, the more difficult

it became to fully remove the excess XT10 from the sample. The largest geometry found to allow all of the XT10 to be removed at the end of the sonic bath was a 5 µm diameter emitter capillary geometry. Again, in Figure 3.15, the excess XT10 is not properly removed once the emitter capillary sizing exceeds 5 µm in diameter. SEM and EDX images were then taken to determine the exact elements that were deposited on the structures, as shown in Figures 3.16, 3.17, and 3.18.

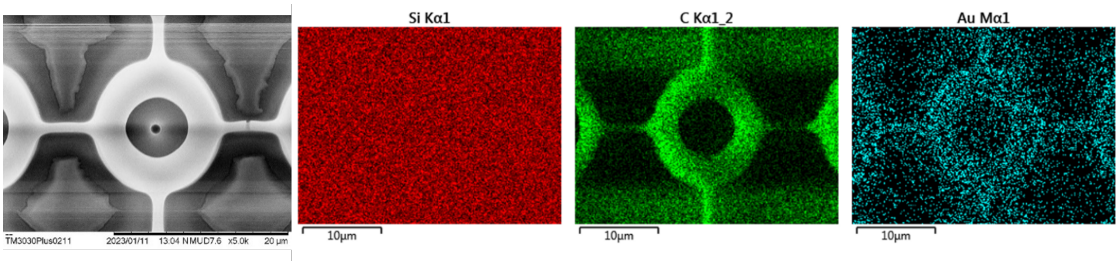

Figure 3.16: SEM and EDX images of 3 µm diameter capillary design.

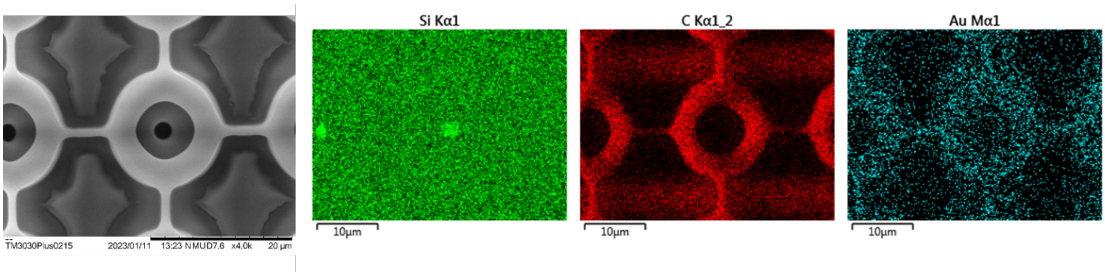

Figure 3.17: SEM and EDX images of 4 µm diameter capillary design.

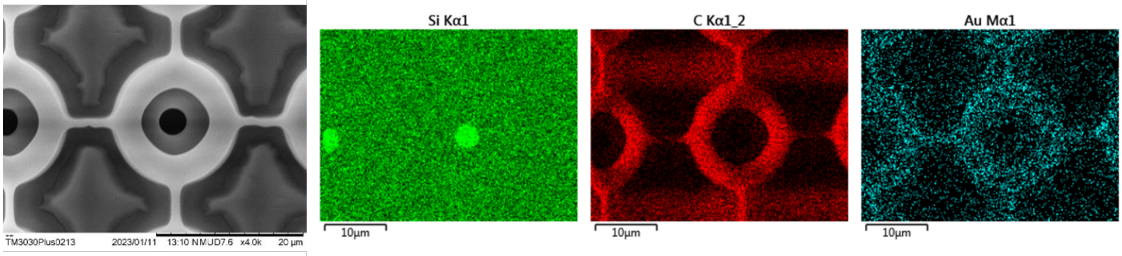

Figure 3.18: SEM and EDX images of 5 µm diameter capillary design.

As the size of the emitter capillary increases from 3 to 5 µm, there are two important differences to be noted in the EDX images in particular. First, the silicon appeared much more strongly as the scale increased within the emitter capillary, indicating that this region

was completely clear of any other material besides the silicon wafer, which is desired. Second, the gold deposition appeared much more directed to the tops of the extractor and fuse regions. This however was due to the thickness of the SU-8 and the precision of the EDX; the EDX was unable to penetrate the 16 µm of SU-8 to differentiate within the 3 µm capillary, which was found when EDX imaging was done on an identical sample that was 10 µm thick instead, consisting of two 5 µm layers instead of two 8 µm layers, as shown in Figure 3.19.

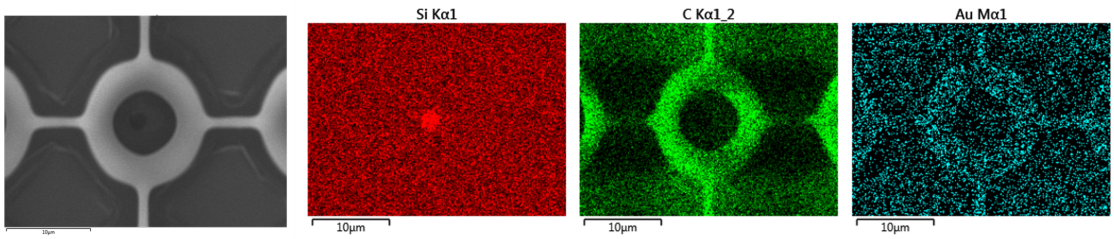

Figure 3.19: SEM and EDX images of 3 µm diameter capillary design with 10 µm thick SU-8.

Therefore, it was concluded that the 3 µm diameter emitter capillary would be open and unclogged using these manufacturing techniques, allowing a 3-5 µm diameter emitter capillary to be used on the array.

3.3.4 Testing of Extractor Conductivity

Though the gold appeared to be thoroughly deposited through SEM and EDX imaging, it was important to ensure that a full conductive path could be made between the extractors and fuses, and to ensure that no excess gold was deposited around the extractors or fuses that could allow for a conductive path between the substrate and the extractors. This was ensured by building a new array model in which the extractors at the ends of the arrays were extended into large 50 mm square surfaces that could be touched using a multimeter, as shown in Figure 3.20.

This was conducted on a 3, 4, and 5 µm diameter emitter capillary design. In between the extended conductive bridges, it was found that there was a connection through the 3 and 4 µm designs, but not through the 5 µm design. This was found to be due to a manufacturing

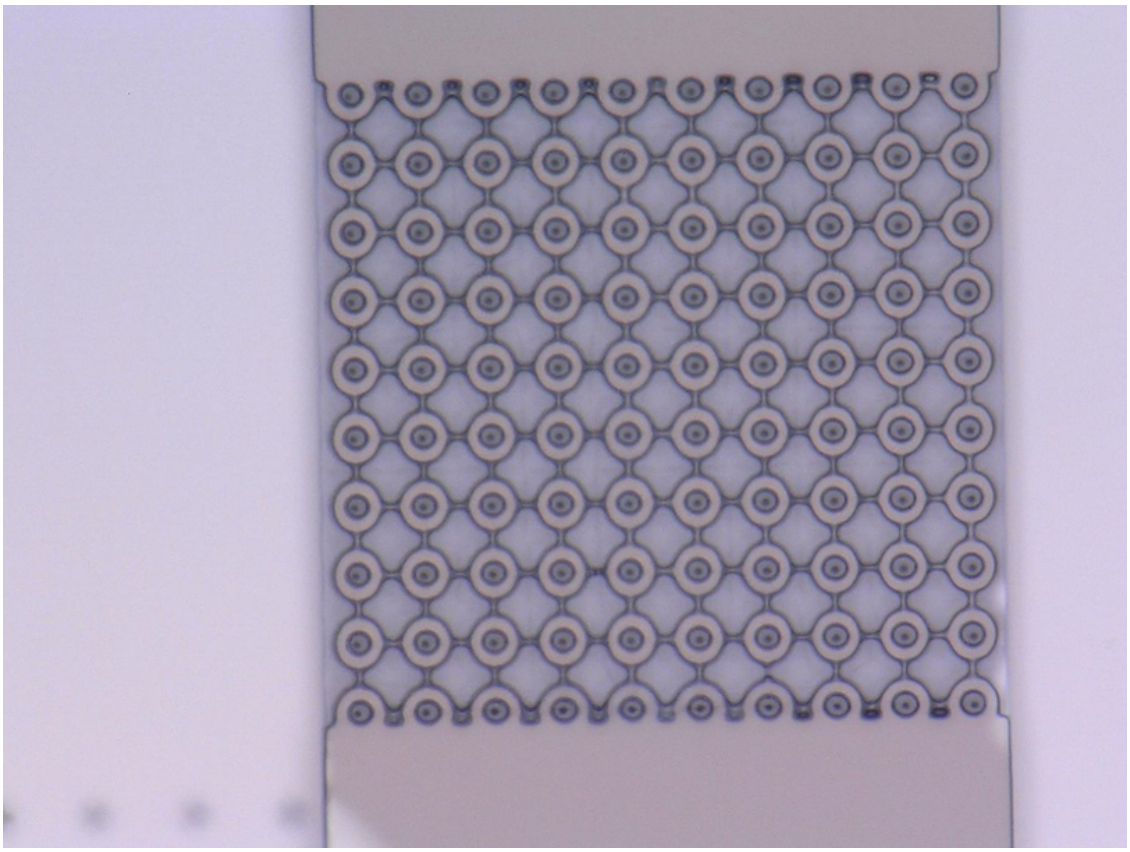

Figure 3.20: 2500x Microscope image of 3 µm diameter capillary design with attached conductive gold bridges.

error in which one of the large extended conductive bridges was damaged. Therefore, it was concluded that as long as there was no excessive damage, the fuses and extractors could be properly connected to one another through a conductive connection. The connection between these extended conductive bridges and the silicon wafer substrate were also tested, and in all three arrays it was found that there was no conductive connection between the arrays and the susbtrate.

3.3.5 Fuse Simulations and Testing

In order to determine proper dimensions for the fuses, a COMSOL simulation was built to test various fuse materials and dimensions to find parameters that would result in the disintegration of the fuses. This simulation used the Joule Heating module, combining

heat transfer and electricity to determine the fuse temperature at a variety of different fuse dimensions and currents. The simulation was built as two rectangular prisms stacked on top of one another, with the lower one representing the SU-8 base and the upper one representing the fuse, shown in Appendix A Figure A.1. A current was applied to one end of the fuse and a ground to the other end. Conduction and radiation conditions were applied to the entire structure, and the base of the SU-8 was set to room temperature. The smallest dimensions found to produce a stable SU-8 structure on the porous glass base, which will be discussed later, was found to be 2 µm wide. To test different fusing materials, the fuse width was therefore set to be 2 µm wide and 10 nm tall, with 10 nm being a reasonable sputter coating thickness. The resulting average fuse temperature was plotted in comparison to the melting and boiling temperature of each, and compared to the fuse temperature if the fuse were free-hanging without an SU-8 bridge underneath to support it. The results for gold and nickel/chromium 80/20 (NiCr) are shown in Figures 3.21 and 3.22, and the results for other simulated materials and the simulation window itself are shown in Figures A.1, A.3, and A.4 in the Appendix.

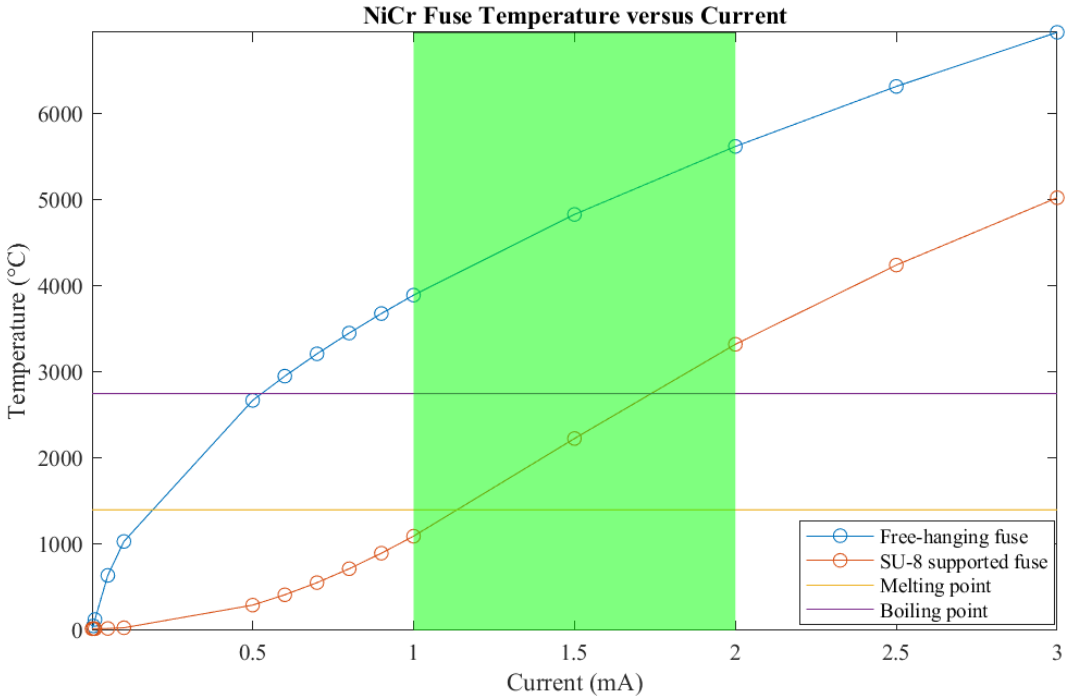

Figure 3.21: COMSOL simulation fuse temperature versus current for NiCr.

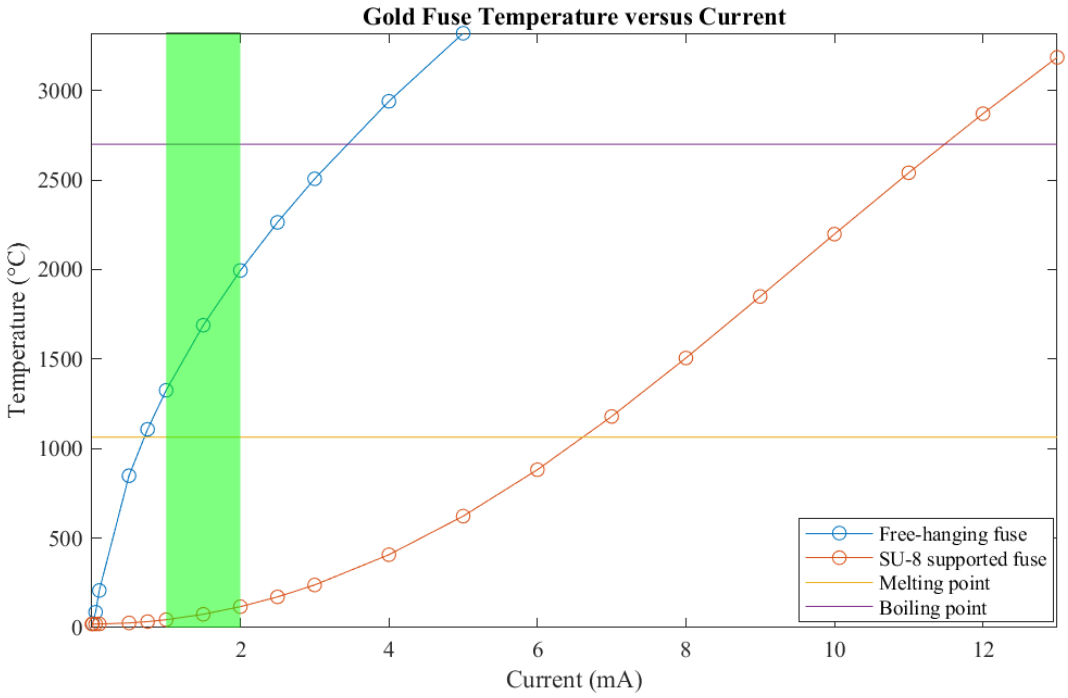

Figure 3.22: COMSOL simulation average fuse temperature versus current for gold.

In Figures 3.21 and 3.22, the green box indicates the current region where the wire temperature should be at least above the melting point, if not the boiling point, of the metal to cause it to fuse. Based on the simulation, it was found that using these dimensions, a NiCr fusing material would be ideal, as at the given geometry of 2 µm wide and 10 nm tall, the fuse would begin to melt at approximately 1.2 mA, and would boil away at 1.7 mA. All of the other metals would require much higher currents beyond the reasonable current range for an electrospray thruster shortage, making NiCr the best candidate.

Next, fuses were simulated with various widths ranging from 2 to 8 µm to determine the effect of cross-sectional area on the fusing current for the SU-8 supported NiCr fuses. The resulting fusing currents are shown in Figure 3.23. Based on these results, the best fusing material was determined to be NiCr, with an ideal width of 2 µm, as this fuse width can be easily manufactured and lies in the desired fusing current range.

To confirm the simulation results, fuse testers were constructed using an SU-8 base with NiCr sputter coated on top for 4 min at 90 W using lift-off using an AJA International

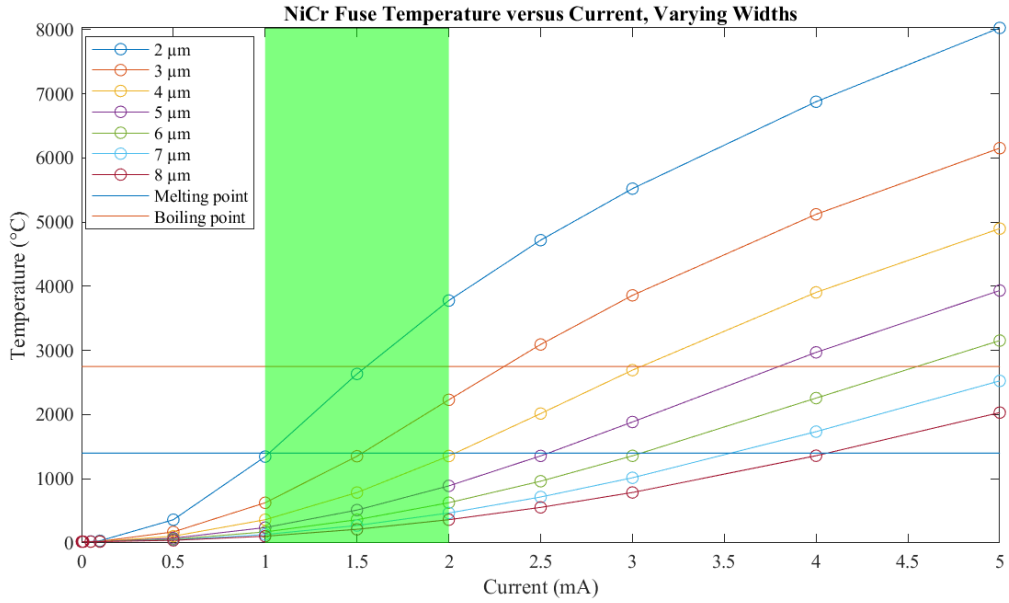

Figure 3.23: COMSOL simulation temperature versus current for 10 nm thick NiCr fuses of varying widths.

sputter coater. The structure consisted of two large pads with a 2 µm bridge between them of lengths 10, 25, or 50 µm. The fuse length should not largely affect the fusing current, however the lengths were varied to determine the manufacturing viability of different fuse lengths. These fuse testers were operated by applying a voltage across the pads, and placing a 10 kΩ resistor in series with a multimeter reading the voltage across the resistor to determine the current. The voltage was steadily increased in increments of approximately 0.01 V until the multimeter stopped reading a voltage. The fusing current was found to vary for each of the testers, with the variance not correlated with the length but likely due to small manufacturing differences, though the fusing currents were in the range of 0.2 to 1.2 mA. This is a lower current than what the COMSOL simulation predicted, and is likely due to a lesser amount of NiCr being deposited than expected, resulting in a fuse with a smaller cross section and therefore a smaller fusing current.

Further experimental testing was completed on various approximately 7 nm thick NiCr fuses with various widths widthsand the average fusing current was recorded in Figure 3.24. The current was applied constantly and very slowly increased until the current was no longer

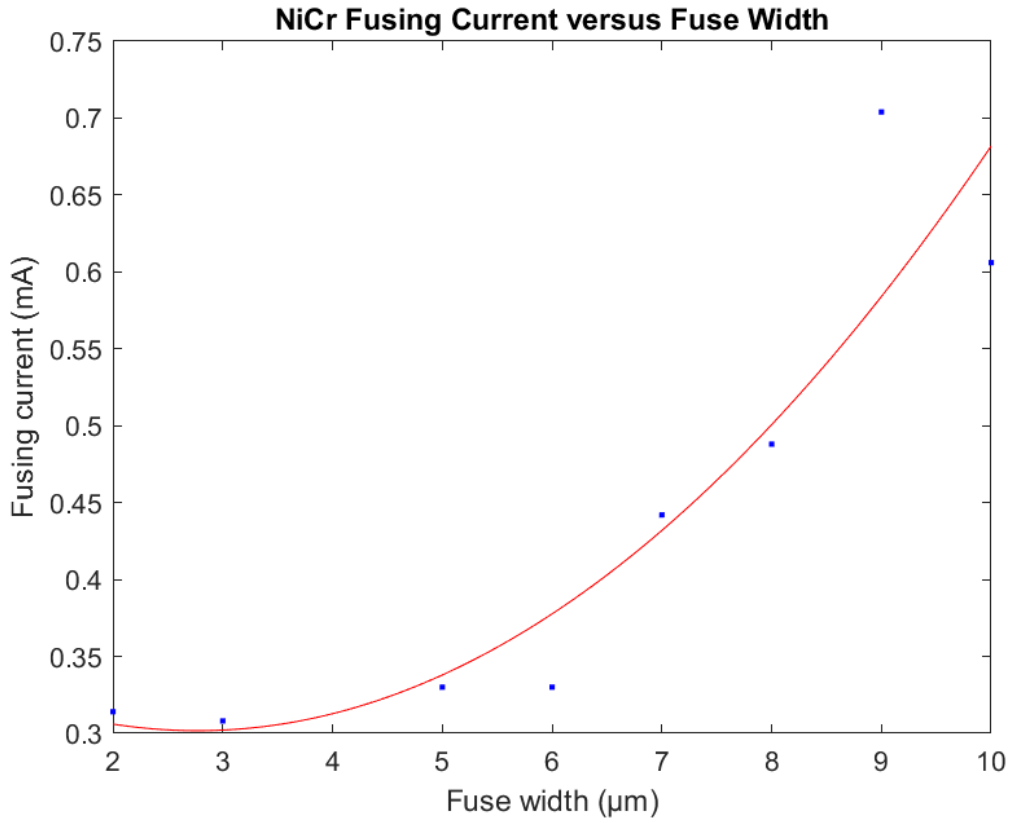

Figure 3.24: Experimental NiCr fuse width versus fusing current recorded for 2-3 fuses tested at each width, with the red-line showing a least-squares regression trend line based on the data.

able to be read across the NiCr fuse. For later testing involving oscillating voltages, approximately 12 nm thick and 2 µm wide NiCr fuses were tested. These experiments were conducted using either a low or high frequency current ramp, which was applied and increased until the fuse broke, leading to similar results that a 2 µm wide NiCr fuse deposited as 10 nm thick would result in a fusing current on the order of 1 to 5 mA. The resulting current reading through the fuses at various frequencies are shown during fusing in Figures 3.25 and 3.26

It is shown in these figures that the fuses can disintegrate relatively quickly upon contact with a current in the desired fusing current range. Though there were some variations in the fusing current experienced in these experiments, they all were in the general desired range to ensure they fuse within the range expected to be experienced during a shortage in an electrospray thruster, which is sufficient for this design. Based on these simulated and

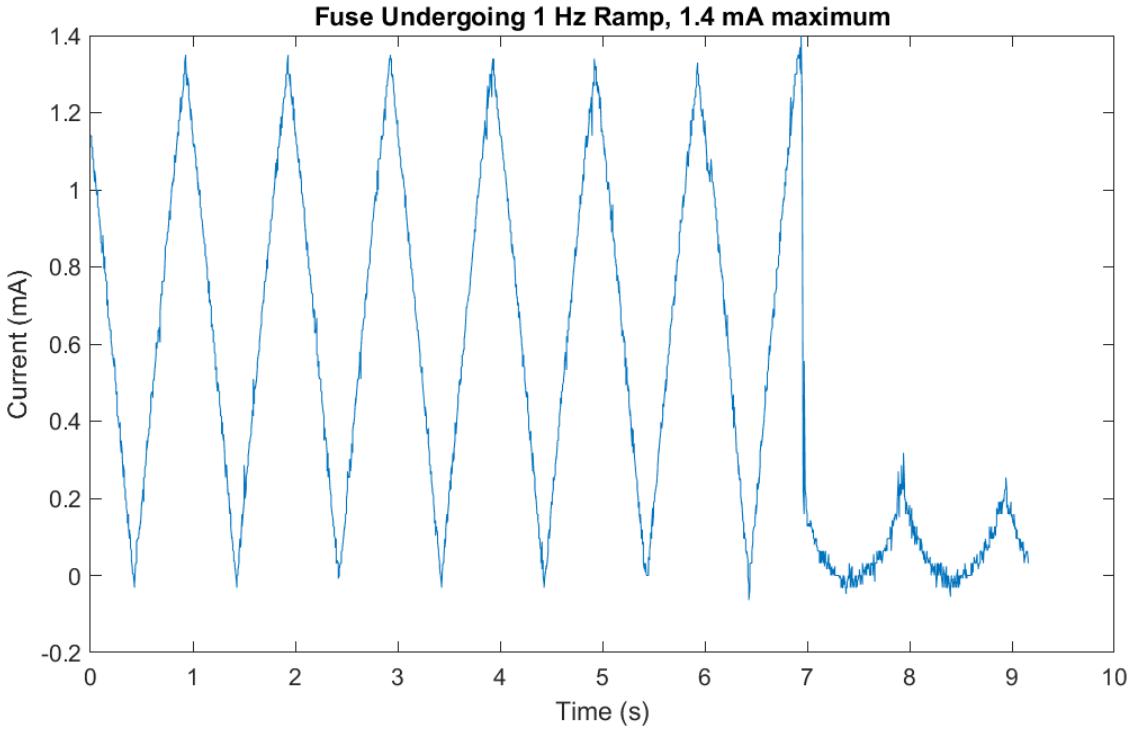

Figure 3.25: 1 s period ramping voltage applied to NiCr fuse with 1 kΩ resistor.

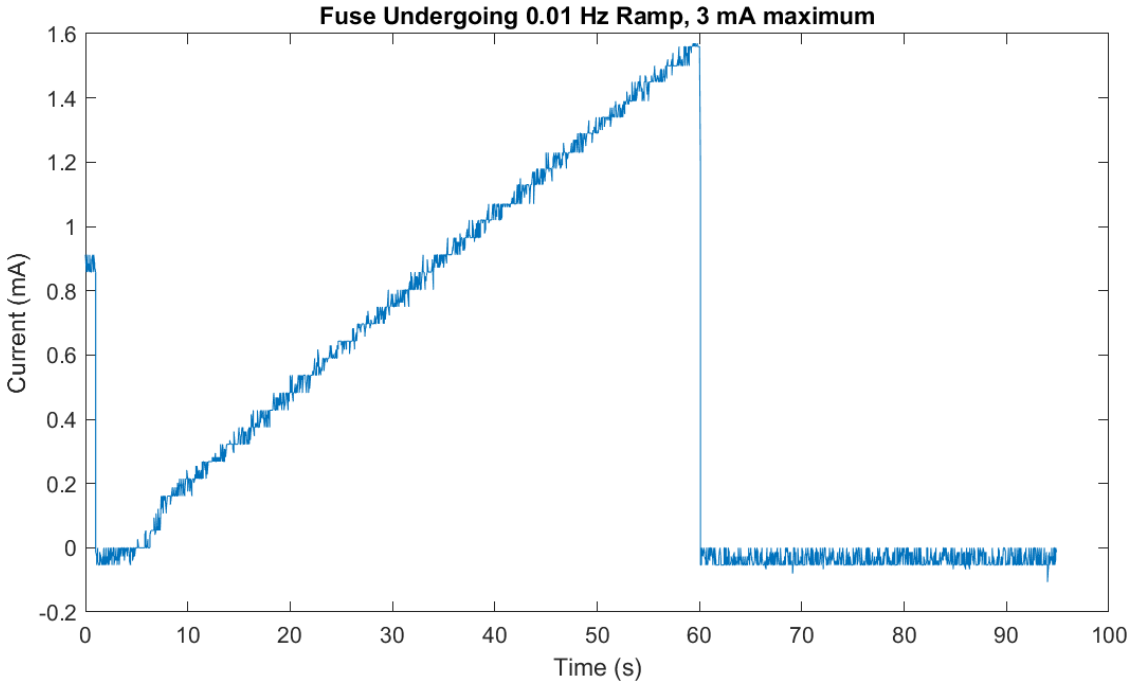

Figure 3.26: 100 s period ramping voltage applied to NiCr fuse with 1 kΩ resistor.

experimental findings, the best fuse material was determined to be NiCr, which should be manufactured to be 2 µm wide and approximately 10-12 nm thick to operate in the desired

fusing current range. To make manufacturing more simple, the extractors should also be made from the same material, but made in regions at least as wide as the fuses to ensure they do not fuse at too low of a current.

3.4 PTFE Coating

Though each emitter will be able to short individually and not affect nearby emitters through the fuse design, it is still important to prevent shortages in any way possible. To help ensure that excess propellant does not pool from the emitter and reach the extractor, a layer of PTFE should be added between these two regions to act as a hydrophobic barrier to prevent shortage of the emitter. To do so, the same lift-off procedure used to apply the NiCr to exact regions to create the extractor and fuse regions was used to pattern sputter coated PTFE (see Figure 3.13); a layer of AZ3312 was applied, exposed, and developed in a pattern consisting of the region between the emitter and extractor regions, PTFE was sputtered, and the excess lift-off and PTFE were removed using an acetone wash in a sonic bath.

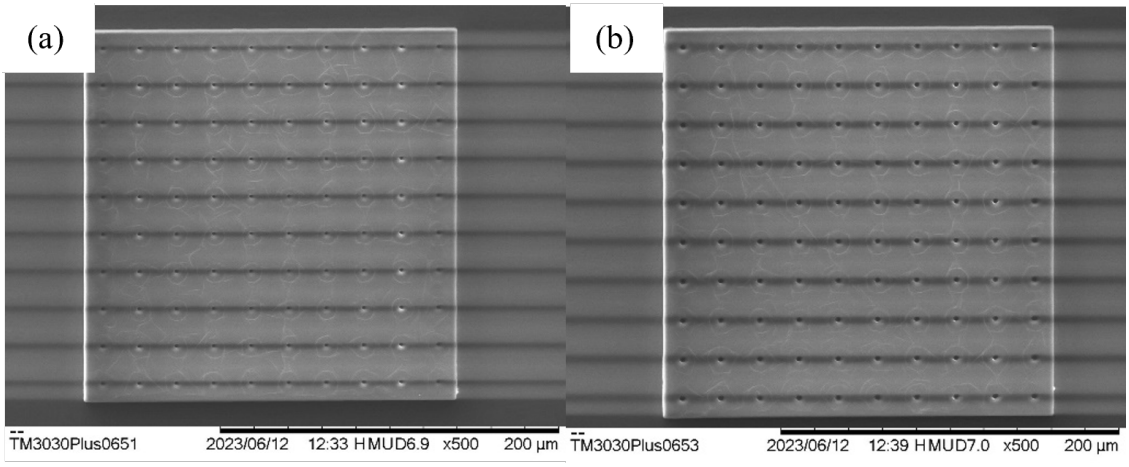

Figure 3.27: SEM images of (a) 5 and (b) 4 µm emitter capillaries with PTFE patterned in regions that would lie between the emitters and extractors.

To determine the emitter and extractor diameter size that would work for allowing proper PTFE deposition, this method was employed on a full two-layer (emitter layer and extractor layer) SU-8 array of varying emitter diameters and extractors, as well as on a single-layer

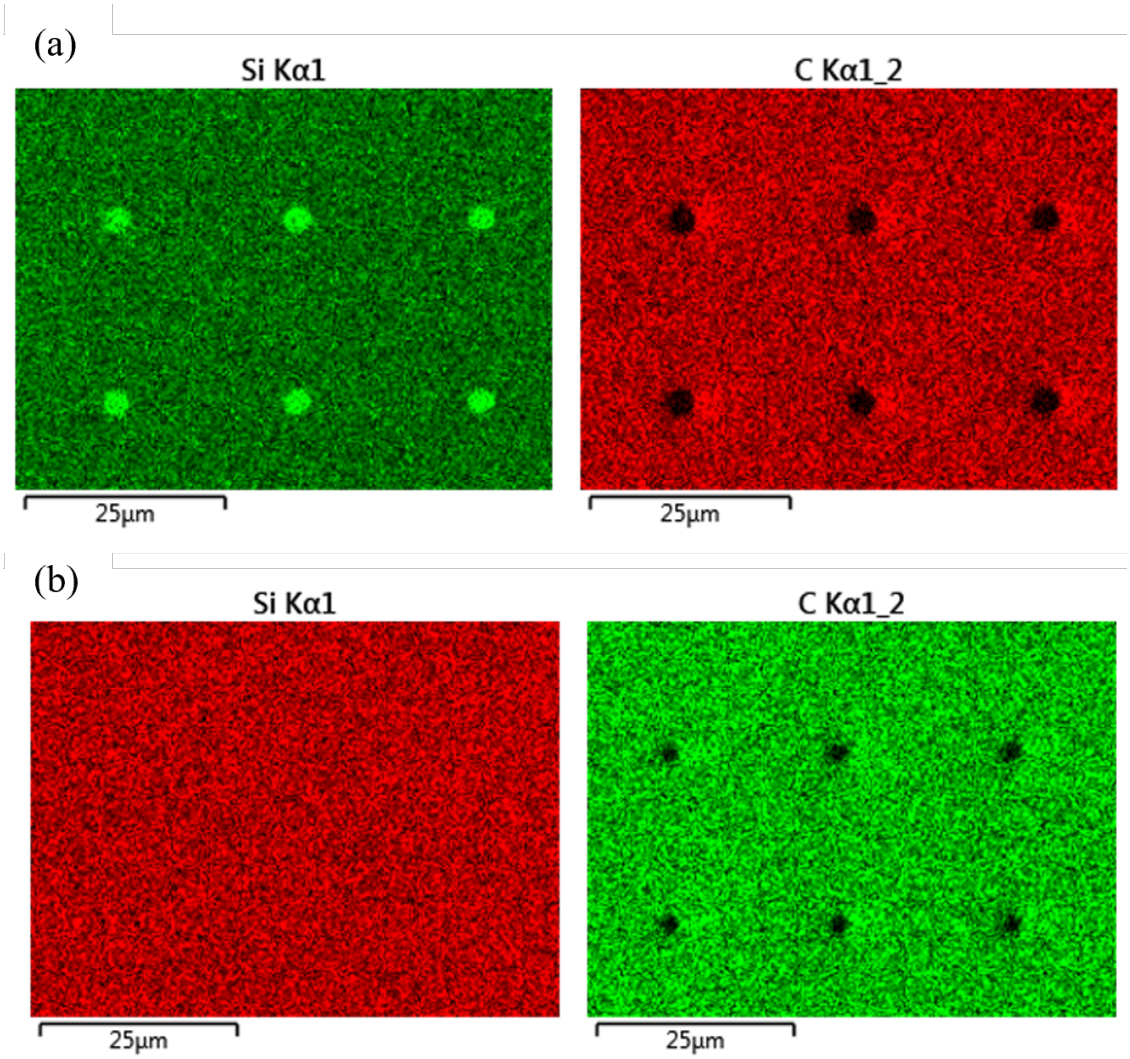

Figure 3.28: EDX images of (a) 5 and (b) 4 µm emitter capillaries with PTFE patterned in regions that would lie between the emitters and extractors.

SU-8 array with only emitters, with the single-layer results shown in Figures 3.27 and 3.28. Because the PTFE layer was so thin, it was difficult to determine its deposition visually on the full two-layer SU-8 array. Therefore, the best diameter size was determined by looking at PTFE patterning on a single-layer SU-8 array, containing only the emitter layer. Though the SEM images suggest that either a 4 or a 5 µm capillary would be properly cleaned of any excess PTFE, the EDX images show that the emitter capillaries are still clogged with PTFE when the emitter capillaries are 4 µm in diameter, but can be properly cleaned when they are 5 µm in diameter. Therefore, though various emitter capillary holes larger and smaller

than 5 µm will still be tested from here, the minimum emitter capillary size that can be used will be 5 µm to allow for proper PTFE patterning.

3.5 Thruster Design on Porous Glass Substrates

To allow the thruster to easily uptake propellant into the emitters, the emitters will be built on a porous substrate. This will require that the substrate on which the thrusters are built simply be in contact with the propellant source, as wetting will allow the propellant to flow up to the emitters through the pores. From here, capillary action and the electric potential of the extractors will allow the propellant to flow up the emitters and begin spraying. The selected material for this process is a porous glass substrate Varapor100, which has pores approximately 100 nm in diameter.

However, using the manufacturing method of spinning and curing SU-8 on the substrate would cause excess SU-8 to enter the pores. Upon initial attempts to spin SU-8 on the surface of the porous glass, sometimes the SU-8 would not seep in and sometimes it would, but its fabrication was generally inconsistent. This is likely because when the SU-8 is added to the surface of the substrate, it is added as a large pool on the surface, then spun at 3000 RPM, and then put on top of a hot plate to set post-spinning. It was very difficult to begin the spin process and post-spin bake process quickly enough before the SU-8 would begin to enter the pores, as it would be sitting undisturbed during these steps and would likely have enough time to begin penetrating the pores. Further, though the substrate was thoroughly developed using propylene glycol monomethyl ether acetate (PGMEA), it is likely that some SU-8 was not exposed to the PGMEA and was not be able to leave the pores, as the pores were on the order of 100 nm in diameter. Further, glass tends to be difficult to complete photolithography on top of due to its refractive properties causing the laser light to scatter during exposure, which will be explained later, and adding opaque material into the glass pores helped to reduce this scattering. Therefore, to remedy these issues, the

pores were filled with fluorene, which is a solid powder at room temperature with a melting point at approximately 116 ^{o}C [64]. The full SU-8, lift-off, and metal/PTFE sputtering was completed on a porous glass wafer saturated with fluorene, then the fluorene was removed from just the surface of the porous glass through sublimation, as will be described in the following section.

3.5.1 VOC Saturation and Sublimation

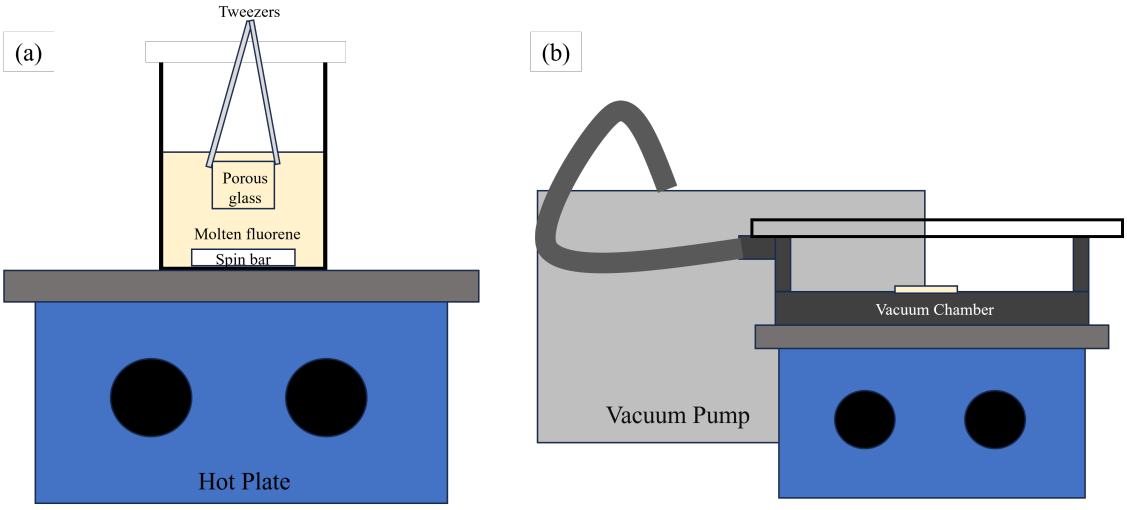

Figure 3.29: Process images for (a) fluorene saturation and (b) sublimation in porous glass.

The fluorene was first melted above its melting point, and the Varapor100 was dipped into the molten fluorene for 2 min to allow it to completely fill the pores of the glass substrate. After this, the glass was spun by hand above the molten fluorene to shake off any excess fluorene. Next, the glass was placed in a desiccator at a high temperature to sublimate a top layer of the fluorene from the surface of the glass. This way, the glass surface would be exposed and there would be no fluorene on it, allowing the SU-8 to stick to the surface of the glass rather than a surface layer of fluorene. This process is shown in the graphic in Figure 3.29. This sublimation was successfully completed when heated and held under weak vacuum for 2 min, and can be seen through the backlit microscope image in Figure 3.30.

Though the sublimation can be visualized at 2 min, a 7 min unheated sublimation time

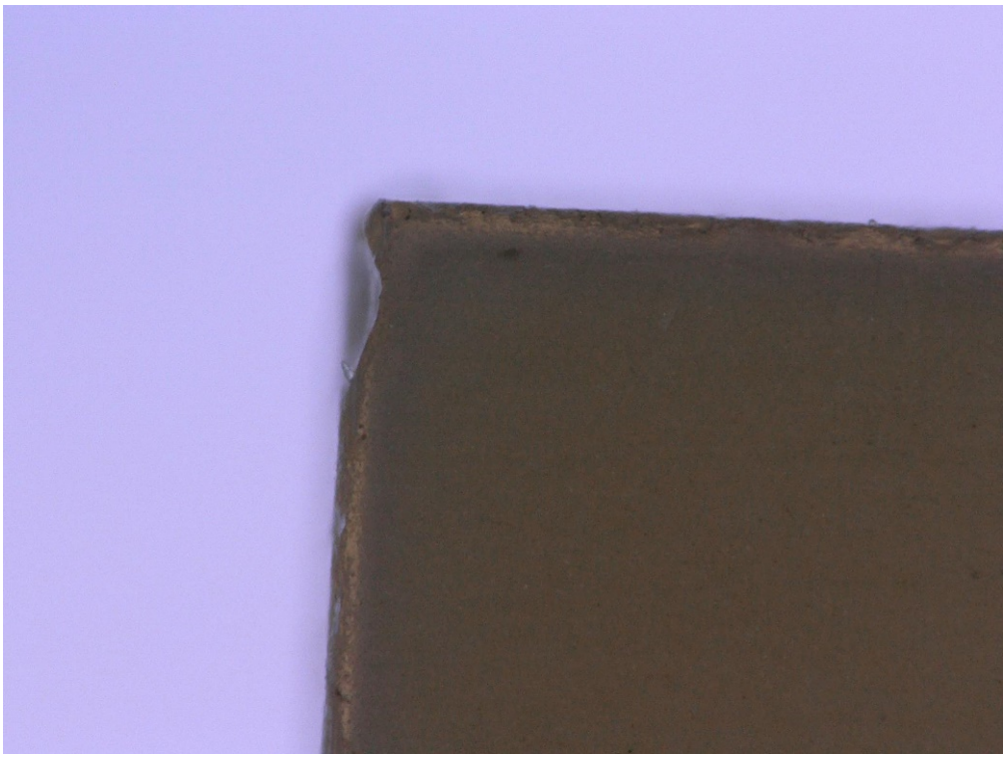

Figure 3.30: 200x Varapor100 substrate saturated with fluorene, post 2 min sublimation.

was necessary for SU-8 manufacturing. After spinning SU-8 on the 2 min heated and sublimated fluorene saturated glass substrate, the SU-8 penetrated too deeply into the substrate. Therefore, a 7 min unheated sublimation was used instead. This timing and lack of heating was determined through varying the temperature and timing of the sublimation. It was found that applying heat caused the sublimation to occur too quickly, resulting in too much fluorene being removed from the top layer of the glass, causing SU-8 to penetrate the pores. Therefore, no heat was applied and the sublimation was completed at various times using a desiccator to apply a weak vacuum, and the ideal sublimation time was found to be 7 min. Though the sublimated layer could not be visualized using the VHX microscope, it was a sufficient amount to allow the spun SU-8 to stick to the glass, without penetrating too deeply into the glass pores. To ensure that the SU-8 was not penetrating the pores too deeply, the fluorene was added to the chip and sublimated for 7 min, SU-8 was spun and cured in the same pattern that would be done for the emitter arrays, the fluorene was removed from the chip, and the chip was then cleaved and a cross section was imaged. The resulting SEM and

EDX images are shown in Figure 3.31.

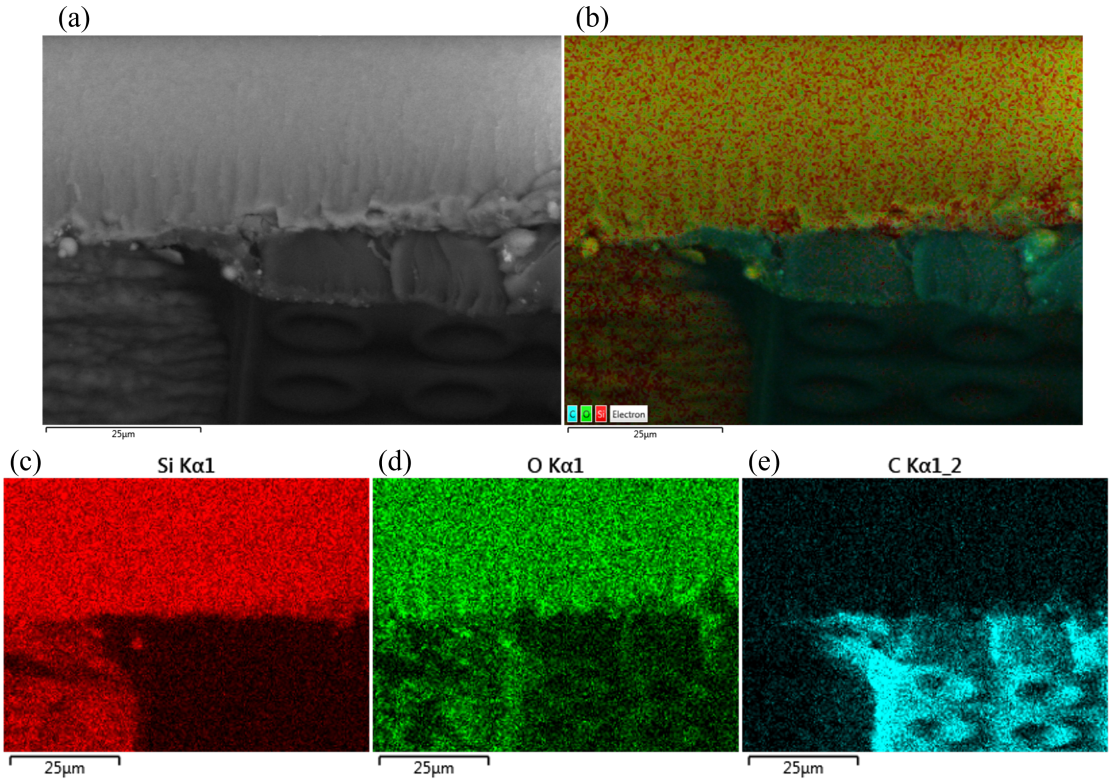

Figure 3.31: (a) SEM, (b) SEM with full EDX overlay, (c) silicon EDX, (d) oxygen EDX, and (e) carbon EDX images of SU-8 on a cleaved Varapor100 chip.

It is apparent that after a 7 min sublimation, the SU-8 can only adhere to the surface of the chip, and does not penetrate deeply into the pores. This is apparent due to the lack of carbon and clearly visible silicon and oxygen in the glass, since fluorene is composed of hydrogens and carbons, while glass is composed of silicon and oxygen.

An alternative VOC, anthracene, was also tested as a material to saturate the porous glass with. The anthracene was similarly melted, the glass was saturated in the solution, and the top layer was sublimated at a high temperature under vacuum. However, the anthracene could not be easily removed from the glass post-manufacturing, likely due to the higher melting point and lower vapor pressure, making fluorene a better candidate. This will be shown later in the thesis.

3.5.2 Fluorene Maintenance during Manufacturing

Because fluorene has such a low melting temperature of 116 ^{o}C, it was important to ensure that the heating processes used during manufacturing did not exceed this so that the fluorene would stay intact. For all post-spin and post-exposure bakes, the temperature was completed at a maximum of 112 ^{o}C, so this would not be an issue. However, the hard-cure process was originally conducted on silicon wafers at 250 ^{o}C for 30 min, as recommended by the manufacturer. To ensure that the fluorene would not melt, the hard-cure would need to be done at a lower temperature, but it would still need to be done thoroughly enough to ensure that the SU-8 structures were stable enough to survive a 10 min sonic bath in acetone, which was required to remove excess lift-off photoresist and gold. This was tested by building the same thruster design as before, but hard-baking at 105 ^{o}C for 1 hr to stay well below the melting point of fluorene. After hard-baking, the substrate was placed in an acetone sonic bath for 10 min, and the resulting SU-8 structures can be seen in Figure 3.32.

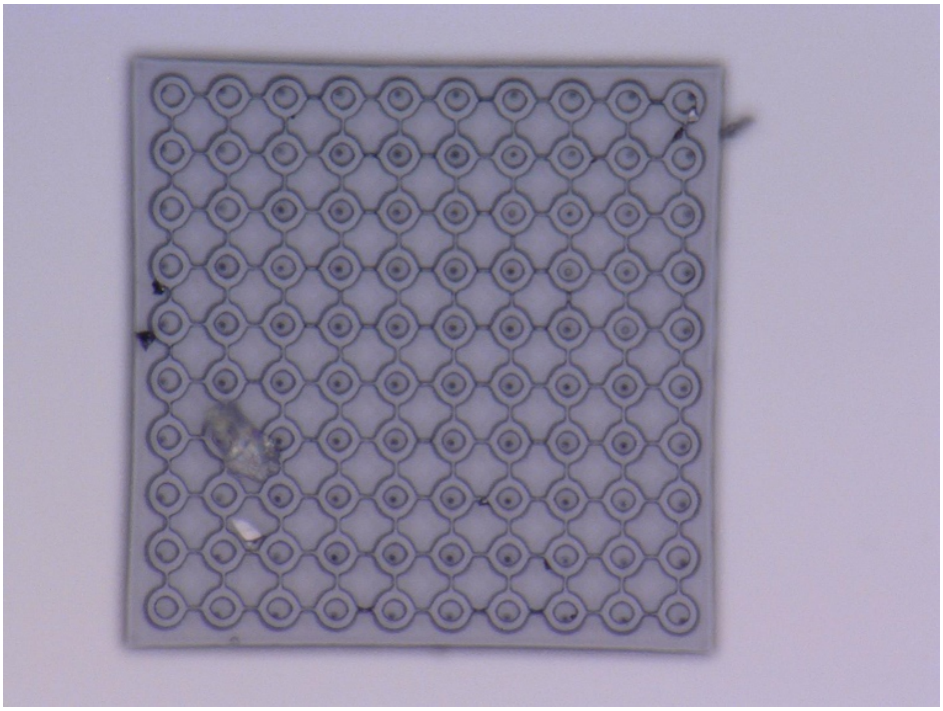

Figure 3.32: Microscope image of 3 µm diameter SU-8 capillary design hard-baked at 105 ^{o}C for 1 hr, post-10 min acetone sonic bath.

It has been shown that the mechanical properties of SU-8 following a hard-bake cycle do not differ much as the temperature increases from 100 to 200 ^{o}C hard-bake temperatures, but it was important to verify this [65]. Though a small portion of the array appears disrupted by a stray piece of material, the array itself held up relatively well after the acetone sonic bath, therefore it can survive the process if necessary. It was later determined that to maintain a more solid structure, a 2 hr cure was ideal to ensure that there was no SU-8 movement, and was used for all porous glass samples in the final process.

3.5.3 SU-8 Manufacturing on VOC Saturated Glass

SU-8 was spun onto the VOC (fluorene) saturated Varapor100 glass wafers, baked, exposed using an MLA, post-exposure baked, then developed in PGMEA. This was done using only the first layer of SU-8 that would be deposited for the array construction to determine how the SU-8 deposits, exposes, and develops on the new susbtrates. On the fluorene and anthracene saturated glass, the resulting SU-8 structures are shown in Figure 3.33 before VOC removal.

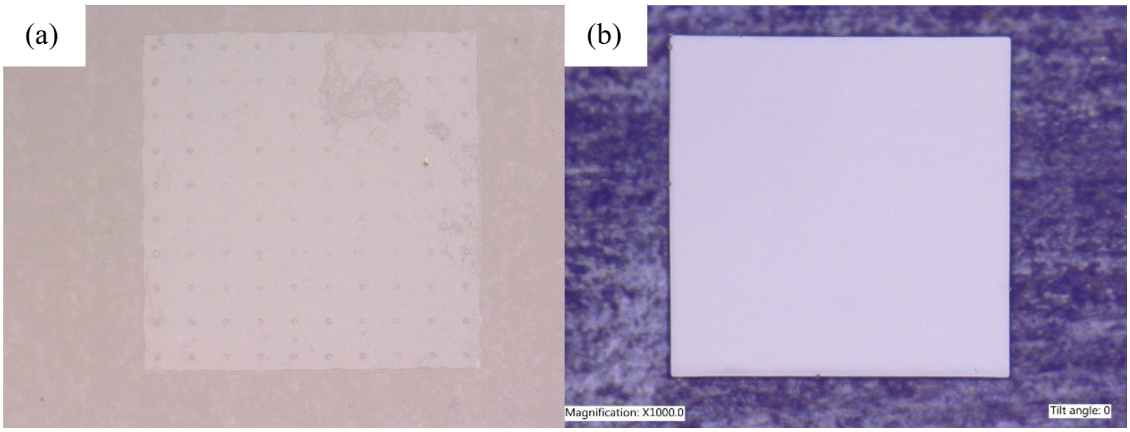

Figure 3.33: 3 µm diameter SU-8 capillaries on (a) fluorene and (b) anthracene saturated Varapor100 glass.

As a result of this deposition, it was determined that the anthracene was causing the SU-8 to sink more into the pores in the emitter hole areas, which would block propellant uptake. Further, it was found to be very difficult to remove the anthracene from the porous

glass post-fabrication, likely due to its much higher melting point of 215 °C and lower vapor pressure. Because of this, the anthracene was removed as a VOC candidate for the process. Though the fluorene emitter capillaries are still a bit clogged with SU-8, they are still visible, and further tuning was pursued to remove the excess SU-8 from these regions.

3.5.4 SU-8 Manufacturing Tuning and VOC Removal

In order to allow the porous glass to uptake propellant, the VOC needed to be removed from the glass post-fabrication. This was done by heating the sample at a high temperature, approximately 200 ^{o}C, under vacuum for 40 min. The resulting sample is shown in Figure 3.34.

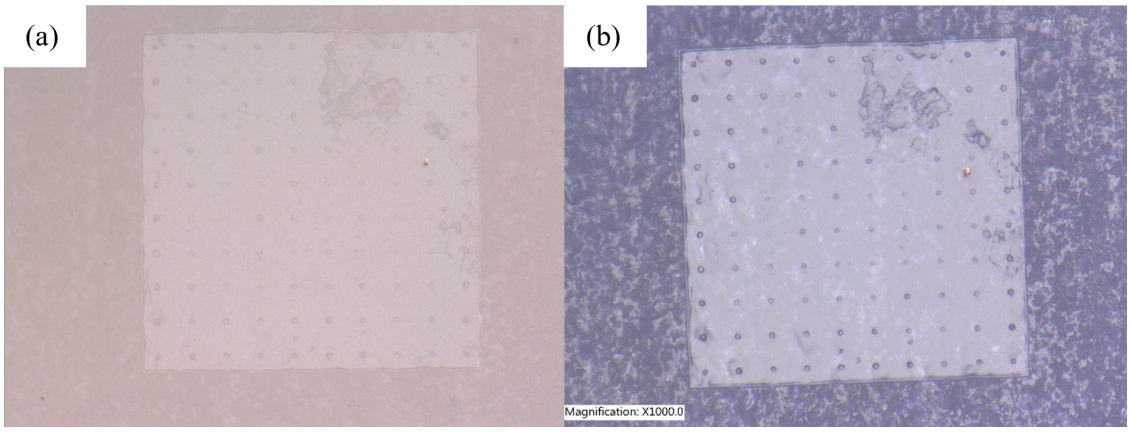

Figure 3.34: 3 µm diameter SU-8 capillaries on Varapor100 exposed with 1400 mJ/cm^2 (a) with fluorene and (b) post complete fluorene removal.

Because of the nature of the fluorene and the porosity of the glass, it was determined that a small amount of SU-8 was penetrating the first layer of the Varapor100 glass more than expected, causing the holes within the emitter to close. This is in contrast with the results shown in the image in Figure 3.35, with an AGC40 glass sample with 40 nm pores being used instead of the 100 nm porous Varapor100.

In both the AGC40 and Varapor100 substrates here, the fluorene was initially sublimated for 30 s with heat after saturation. However, because the AGC40 pores are smaller, less fluorene was removed from the pores near the surface of the glass, preventing the SU-8 from

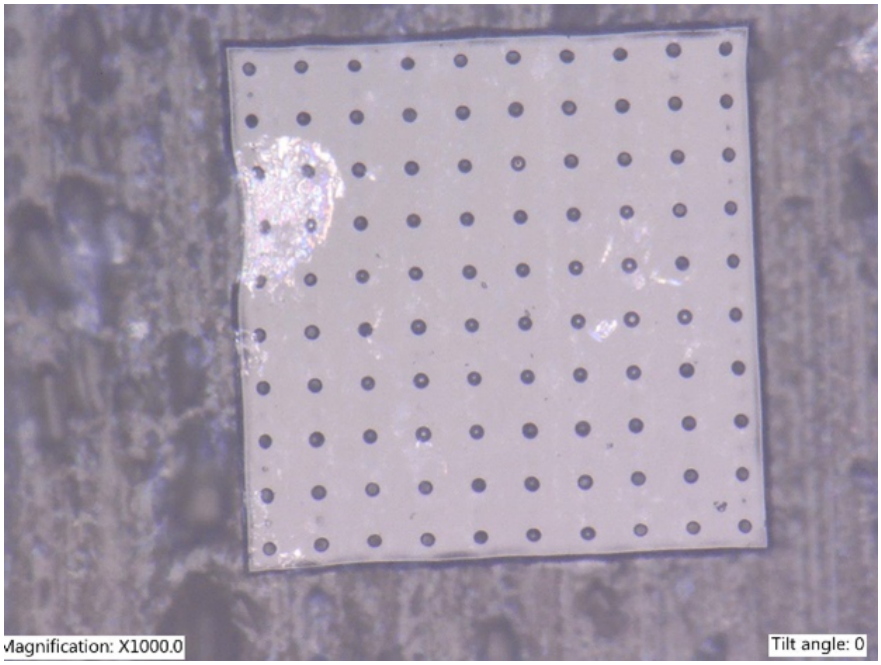

Figure 3.35: 4 µm diameter emitter capillaries exposed with 1300 mJ/cm^2 on fluorene-removed AGC40 glass.

penetrating the pores of the glass, allowing it to be properly removed more easily than in the Varapor100 samples with larger pores. Using EDX and SEM imaging, it was found that the best exposure dosage for the SU-8 that would still allow the structure to be intact while allowing the emitter capillaries to remain clear was 1100 mJ/cm^2 on AGC40. The SEM and EDX images corroborating this conclusion are shown in Figure 3.36.

As shown clearly in Figure 3.36, the carbon is only present in the regions where the SU-8 is present, while there are spikes of silicon where the glass beneath is exposed through the empty emitter capillaries. Unfortunately, due to supply chain issues, further experimentation was completed using solely the Varapor100 glass samples, so the manufacturing issues associated with this substrate had to be resolved.

To solve the issue of too much fluorene sublimation in the Varapor100 100 nm porous glass susbtrates, the glass was sublimated for varying amounts of time only under vacuum, without any additional heat applied, as previously mentioned. Because fluorene has a low vapor pressure, the fluorene could still be sublimated given a sufficient vacuum, however the

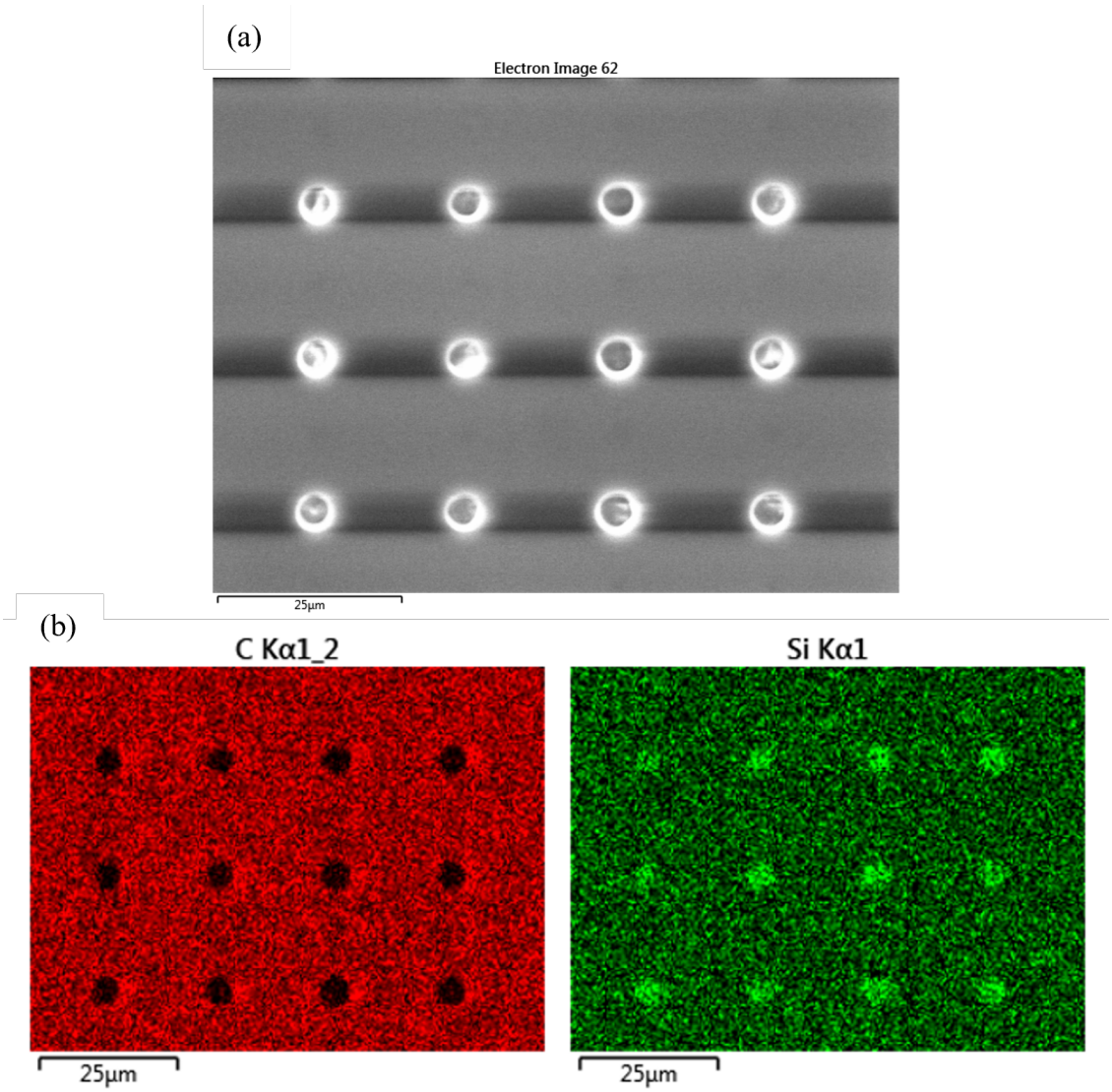

Figure 3.36: (a) SEM and (b) EDX images of 4 µm emitter capillary SU-8 structures exposed with 1100 mJ/cm^2 dose on AGC40 post fluorene removal.

sublimation occurred much more slowly than when heat was additionally applied, allowing the sublimation to occur more slowly and more controllably. Through testing, a 7 min sublimation time only under vacuum at room temperature was found to remove fluorene from just the surface and much less from within the pores near the surface of the glass, allowing for smaller emitter capillaries to be manufactured without being filled with SU-8. This was determined through increasing the sublimation time until SU-8 would be able to adhere properly to the surface after spinning, meaning that only the top layer of the substrate

had been cleared of fluorene. This is shown in Figures 3.37 and 3.38.

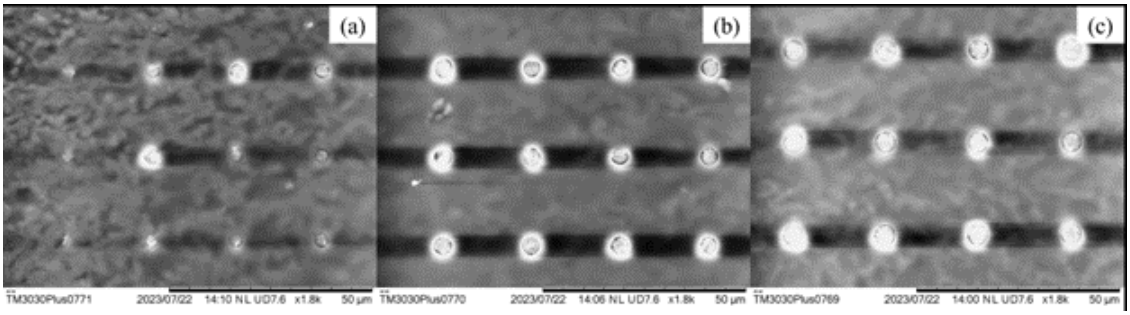

Figure 3.37: SEM images of (a) 3, (b) 4, and (c) 5 µm emitter capillary SU-8 structures exposed at 500 mJ/cm^2 post 7 min fluorene sublimation under vacuum at room temperature.

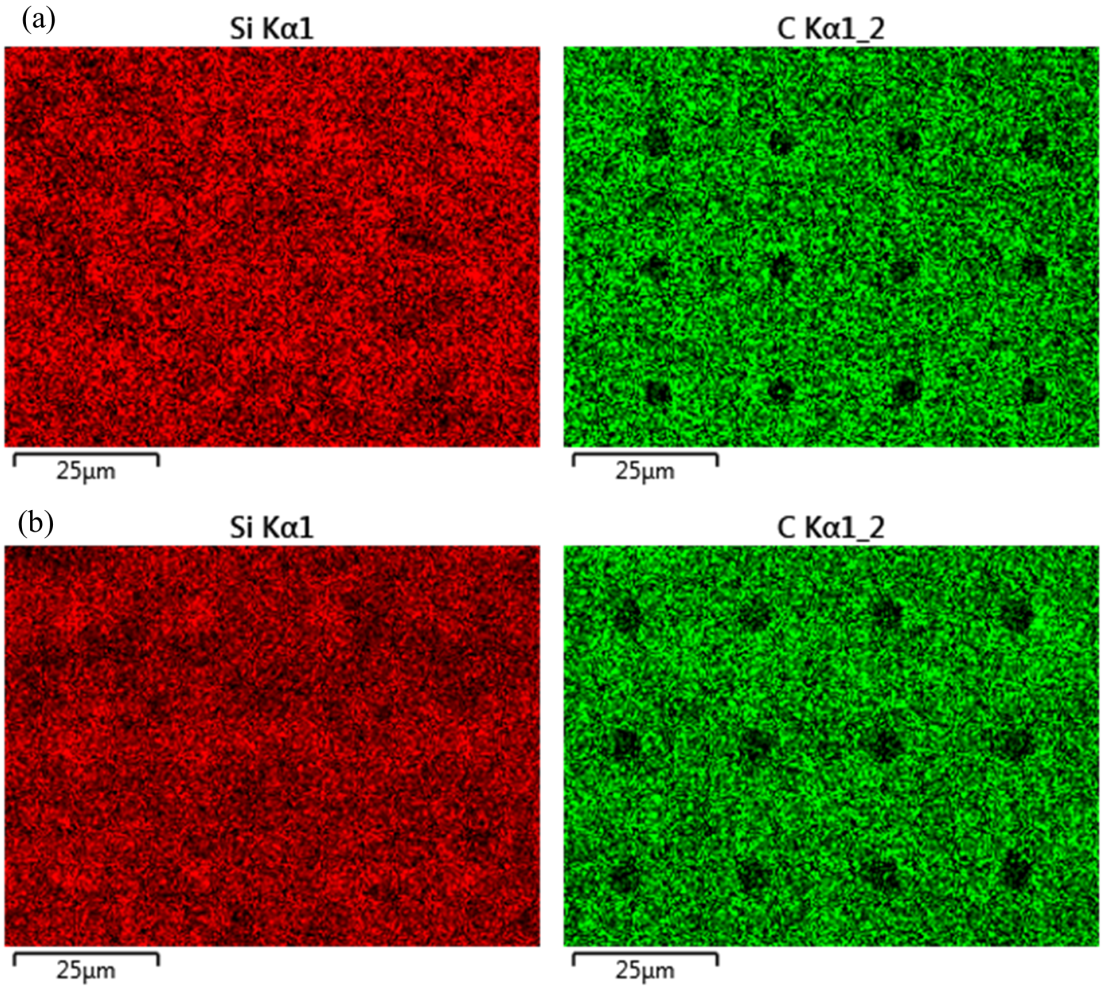

Figure 3.38: EDX images of (a) 4 and (b) 5 µm emitter capillary SU-8 structures exposed at 500 mJ/cm^2 post 7 min fluorene sublimation under vacuum at room temperature.

From here, because the design was capable of producing a single layer of SU-8, the full

array structure was built as explained in earlier sections on the Varapor100 porous glass samples. However, because of the properties of the glass, the XT10 thick photoresist layer was unable to properly expose and develop using the previously used settings for the silicon wafer process. Because of this, the XT10 was replaced with AZ3312, which is a thinner photoresist that was spun to approximately 1.5 µm and was able to expose and develop more cleanly. A fully constructed 5 µm emitter capillary diameter array on Varapor100 with NiCr-deposited fuses and extractors and a PTFE coating in between the emitter and extractor region is shown in the following figure. To ensure that the fluorene was fully removed and the glass could be wetted, the chip was placed in a puddle of EMI-Im propellant, also shown in Figure 3.39.

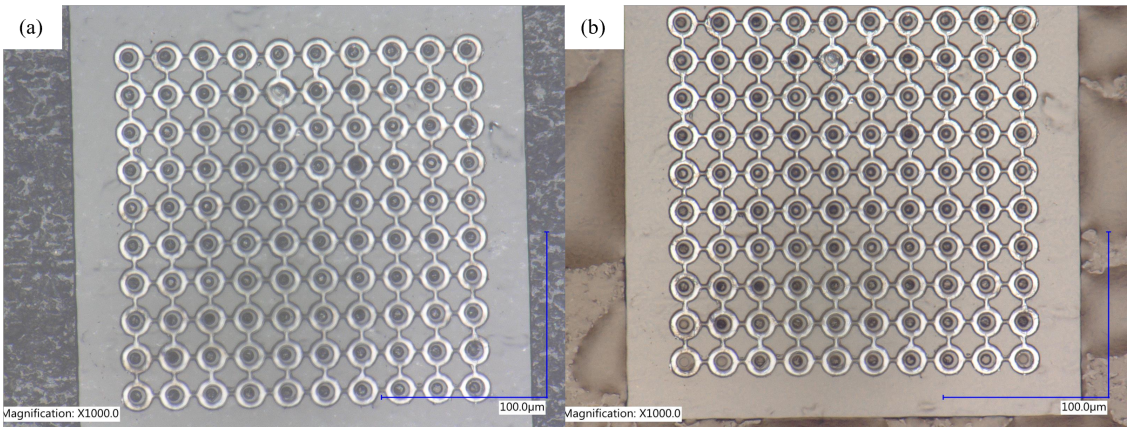

Figure 3.39: 1000x VHX Microscope image of SU-8 thruster with NiCr extractors and fuses applied on Varapor100 (a) post-fluorene removal and (b) post-propellant wetting.

As shown in Figure 3.39, when looking in particular at the top right emitter, before wetting the surface texture of the glass is visible, while after wetting the emitter becomes a lighter color with no texture, indicating it is filled with propellant.

3.5.5 SU-8 Manufacturing Scale-up

The structures built in the previous sections were only built using small areas of SU-8. This was done for preliminary testing to see if small, 10 by 10 arrays could be manufactured, and only an area that was a 300 µm was at most manufactured. However, when a full thruster

is manufactured, any open areas on the substrate surrounding the emitters will need to be coated in a layer of SU-8 on the entirety of the thruster chip to prevent any propellant from potentially wetting to the surface in undesired regions outside of the emitters. Therefore, large areas of SU-8 will need to be cured around the emitters.

Though this initially was not perceived an as issue, when manufacturing began that involved building several emitters across the entire susbtrate and exposing large areas of SU-8 between the emitters, an excessive cross-linking effect was observed. Essentially, when SU-8 is exposed on glass specifically, due to its refractive properties, as larger areas and thicker layers of SU-8 are exposed at a time, the edges of the exposed pattern begin to cross-link in larger areas surrounding the desired exposure pattern, which has been previously recorded in literature [48].

This caused a worsening of the emitter blockages due to undesired SU-8 cross-linking occurring within the unexposed emitter regions. When these larger areas of SU-8 were exposed in a single exposure step around the emitters, the excessive cross-linking effect started to spread into the emitters, resulting in them becoming completely clogged with cured SU-8. As briefly mentioned earlier, when this process was completed on porous glass substrates without fluorene, this effect was significantly exasperated, and filling the pores with fluorene prior to SU-8 fabrication helped to reduce this issue by reducing the amount of scattering within the substrate during laser exposure.

To better understand this issue, and try to ameliorate it by dividing the large exposure area into smaller areas exposed in separate exposure steps, concentric rings of SU-8 were cured with unexposed gaps between them in a single exposure step to ensure that a large continuous area of SU-8 was not exposed all at once. To determine the necessary sizing and dosage conditions to allow the SU-8 cross-linking to only occur in the exposed regions, a series of rings with different widths, spacings, and exposure dosages were built, with some notable examples shown in Figure 3.40.

Here, you can imagine the spacing between the exposed rings as the emitters, with the

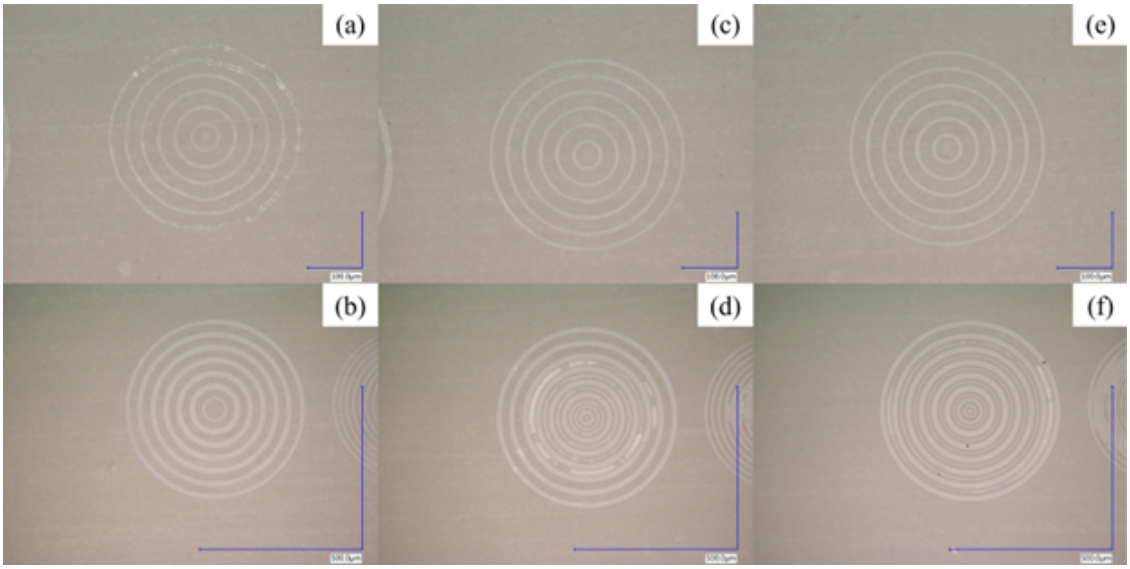

Figure 3.40: Microscope imaging of rings of SU-8 on fluorene filled Varapor100, with (a, c, e) 10 µm wide rings spaced 20 µm apart, (b, d, f) 20 µm wide rings spaced 20 µm apart, exposed at (a, b) 600 mJ/cm^2, (c, d) 800 mJ/cm^2, and (e, f) 1000 mJ/cm^2.

rings themselves representing areas that are exposed around them. As shown, by exposing the structures at a higher dosage, or spacing the structures closer together, excess SU-8 begins to cross-link between the structures, clogging the 5 µm emitter in the center of each set of concentric rings. This is seen as the area between the concentric rings no longer having the more dull and textured color and pattern of the glass, and instead having a smooth, brighter appearance consistent with the SU-8. However, it is important that the SU-8 is exposed at a high enough dosage to allow for the structures to be sharper in shape and clarity. Therefore, the best ring width, spacing, and dosage for the first layer of concentric rings was determined to be 10 µm wide areas with 20 µm spacings exposed at 800 mJ/cm^2. However, upon spinning a second layer of rings, the central open emitter in the middle of the rings still began clogging. This is likely because it was still too large of an area that was being exposed, and also the substrate had already been developed, and it is possible that the development caused some fluorene to be removed from the surface pores of the glass, allowing the emitter to clog with SU-8 more easily. Because if this, the resulting manufacturing process required that a central ring of SU-8 be fabricated first with a maximum outer diameter of 70 µm, then

each following concentric ring 50-100 µm can be individually fabricated after, until an outer diameter of approximately 350 µm was reached, after which point the rest of the chip could be coated with SU-8 and exposed without risking the emitter's integrity. It was important that the central ring, where the meniscus would pin, was done in the first set of rings at the highest possible dosage to ensure the structure has sharp corners for the meniscus to pin to.

Alternatively, it was found that following the fabrication of the first SU-8 ring immediately around the emitter, the rest of the substrate could be coated instead with PTFE to prevent wetting, rather than SU-8. This method allowed for the complete avoidance of the clogging issue altogether. It also took much less time to fabricate an emitter using this method instead of the previously described method. The previous method would require about 4-5 repeated rounds of spinning, baking, exposing, post-exposure baking, and developing SU-8 on the substrate, each round taking approximately 1 hr to complete. However, this method only required a single round of SU-8 fabrication, followed by applying a lift-off layer and sputtering PTFE which needs to be done in either case anyway to apply a PTFE ring around the emitter to prevent the propellant in the capillary from wetting to the SU-8 surface. The only material difference in this method was that instead of using a positive photoresist for the lift-off material, such as AZ3312 that was previously used, a negative photoresist lift-off was used, that being AZ nLOF 2020. As previously noted, a negative photoresist is better to use when the desired remaining patterned portion is smaller than the portion that is to be removed (or in the case of lift-off, the area that is to be sputtered on), since this will require less exposure time and area. Since a large area of PTFE would need to be sputtered on for this process, a negative lift-off photoresist was better to use, so AZ nLOF 2020 was used in a similar way, which involved exposing the smaller emitter areas that PTFE coating was not desired to keep those areas coated and protected during PTFE sputter coating. An example of both fabrication methods is shown in Figure 3.41, and additional SU-8 can be processed on top later to add the bases for the extractors and fuses.

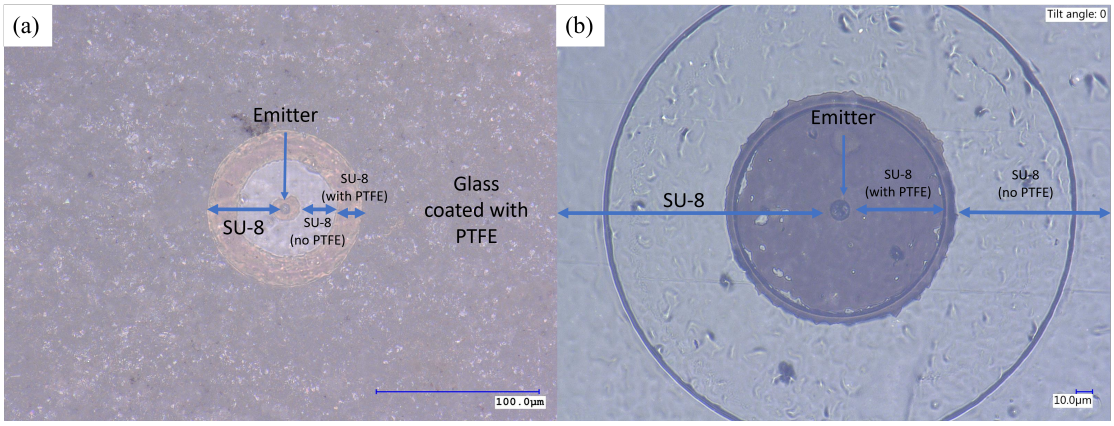

Figure 3.41: Microscope imaging a pixel emitter manufactured using (a) PTFE and (b) SU-8 to cover excess glass surface.

3.6 Final Thruster Design

The final thruster array design consists of an SU-8 thruster with NiCr deposited to the extractor and fuse regions using AZ3312 positive photoresist lift-off and PTFE deposited to add hydrophobic regions to the thruster. The full process for this design is detailed in Table 3.1.

Process	Process Steps	Tool
1. SU-8 Base/Emitter	a. 5 µm SU-8 2005 spin coat (30 sec spin at 1050 rpm) and bake 5 min at 105 °C.	Spinner-SU8
	b. SU-8 exposure of emitters and crosshairs at 600 mJ/cm^2 with 375 nm laser and post-exposure bake 10 min at 105 °C.	DirectWrite-MLA150-AirAF
	c. 30 sec SU-8 development in PG-MEA.	Spinner-SU8

	d. Optional: Repeat a. through c. 3 times to add rings of SU-8 and coat entire chip, using 3000 RPM spin coat speed and 350 mJ/cm^2 exposure dosage.	Spinner-SU8, DirectWrite-MLA150-AirAF
2. AZ nLOF 2020 Lift-off	a. 1.5 µm resist coating (1 min spin at 3000 rpm), bake 112 °C 2 min. b. Exposure of AZ nLOF resist at 800 mJ/cm^2 with 405 nm laser and post-exposure bake 90 s at 112 °C. c. Development of AZ nLOF 2020 layer in AZ300.	Spinner-Resist-U12 DirectWrite-MLA150-AirAF Develop-Hood
3. PTFE Sputter Coating	a. Sputter approximately 20 nm of PTFE on wafer, 30-45 min sputter at 60 W.	SPL Sputter coater
4. AZ nLOF 2020 Removal	a. Rinse/1 min sonic bath in acetone.	Sonic bath
5. SU-8 Extractors/Fuses	a. 8 µm SU-8 spin coat (30 sec spin at 1050 rpm) and bake 5 min at 105 °C. b. SU-8 exposure of extractors and fuses at 400 mJ/cm^2 with 375 nm laser and post-exposure bake 10 min at 105 °C. c. 30 sec SU-8 development in PG-MEA. d. SU-8 hard-bake/cure, 105 °C for 2 hr.	Spinner-SU8 DirectWrite-MLA150-AirAF Spinner-SU8 Spinner-SU8

6. AZ3312 Lift-off	a. 1.5 µm resist coating (1 min spin at 3000 rpm), bake 112 °C 5 min. b. Exposure of AZ3312 resist at 800 mJ/cm^2 with 405 nm laser. c. Development of AZ3312 layer in AZ300.	Spinner-Resist-U12 DirectWrite-MLA150-AirAF Develop-Hood
7. NiCr Sputter Coating	a. Sputter 10-15 nm of NiCr on wafer, 4 min sputter at 90 W.	SPL Sputter coater
8. AZ3312 Removal	a. Rinse/1 min sonic bath in acetone.	Sonic bath
9. Fluorene Removal	a. Place in desiccator under vacuum on hot plate set at 150 °C for 2 hr. b. Rinse/5 min sonic bath in acetone, rinse/1 min sonic bath in isopropanol.	Hot plate/Desiccator Sonic bath

Table 3.1: Full thruster fabrication process table.

The dimensions used for the design consist of a 3-5 µm diameter emitter capillary that is 8 µm long, with either a full surface coating of 5 µm thick SU-8 or 20 nm thick PTFE. In either case, the emitter is surrounded by an extractor base which is an 8 µm thick layer of SU-8, with PTFE between the emitter and extractor regions. The SU-8 extractor base is coated with approximately 10 nm NiCr deposited on top to serve as the extractor. The extractors are connected to one another through a series of fuses on elevated regions of SU-8 also with thickness 8 µm and width of 2 µm, also coated in 10 nm thick NiCr.

Chapter 4

Conclusion

This thesis focuses on the determination of manufacturing parameters to fabricate high resolution micron-scale SU-8 structures, with patterned and sputter coated PTFE and NiCr on porous glass for electrospray thruster applications. Advancements were made in the ability to build flat surfaces on porous substrates through the saturation of a VOC within the porous material prior to fabrication. This method can be applied to building a variety of microfluidic devices, particularly for the length scale required to manufacture a flat panel electrospray array.

4.1 Manufacturing on Porous Glass

Porous materials, particulary porous glass, are very useful substrates because of their ability to easily uptake and transport fluids, heat, and vibrations, making them especially useful in microfluidics applications. Though there has been ample research into the fabrication of porous materials, and even patterning into some porous materials, there has been no research covering the manufacturing of microstructures on the surface of a porous material. This can be extremely beneficial for a variety of applications, as it can allow a porous substrate to uptake a fluid, and then direct it more precisely using the structures manufactured on top.

This manufacturing was completed by saturating porous glass with a VOC, fluorene,

which has a high vapor pressure and low melting point, but is still solid under standard conditions. Due to its properties, it could be easily saturated into the pores of the glass substrate, and remain solid throughout surface fabrication processes. The substrate was then augmented through the spin coating, exposure, and development of a variety of structures built using SU-8, and lift-off was properly completed on top of the SU-8 to pattern PTFE and NiCr coatings, all on a porous substrate.

Following fabrication, the VOC was removed through sublimation by letting the sample sit under vacuum at high heat, without disrupting the SU-8, PTFE, or metallic structures built on the surface. Though further recipe tuning is necessary to get higher feature resolution, this is a first step towards building micron-scale structures on top of porous materials.

4.2 Electrospray Thruster Design

4.2.1 Manufacturing

The main goal of this thesis was to build structures on top of porous glass specifically for electrospray thruster design purposes. Electrospray thrusters are extremely efficient space propulsion devices that allow for a very high specific impulse and low thrust, making them useful in long duration spacecraft missions. However, they lack in their ability to be manufactured at a proper scale to allow for full PIR emission, and often have short lifetimes due to shortage issues. These issues can be fixed through the manufacturing of a flat-panel capillary electrospray emitter array, fired using a fuse-connected series of extractors.

This thesis provides proof of viable fabrication methods to build these devices, by manufacturing a flat SU-8 surface on top of a porous material. The porous glass can uptake the propellant, and direct it to the SU-8 emitters built on the glass surface. Further, these emitters can be built at a length scale and with materials that agree with theoretical parameters necessary for PIR emission. Additionally, the SU-8 emitters can have a PTFE layer added to prevent propellant pooling, and an integrated NiCr extractor array can be manufactured

directly on the thruster chip, with fuses built at a length scale conducive to fusing at currents associated with thruster shortage.

4.2.2 Future Steps

There is much work to be done to continue manufacturing, testing, and optimizing these "pixel" arrays. Following proper manufacturing and characterization of the SU-8 on porous glass, a single emitter will need to be built and fired using a standard non-integrated extractor to ensure complete propellant uptake, PTFE aid in preventing fuel pooling, and PIR emission. Once this can be tested and verified, integrated extractors will be added to these single emitters to ensure that the extractor design can operate properly and does not cause early emitter shortages. Next, larger arrays will need to be manufactured and tested to ensure the proper firing of multiple emitters, and the proper functioning of the fuses following an emitter shortage. From here, the arrays will need to be optimized in sizing to allow for the most efficient emission and longest lifetime possible. Testing will consist of firing the thrusters in vacuum chambers, and taking time-of-flight measurements to determine the species within the plume, as well as retarding potential analyzer measurements to determine the energy distribution of the plume. It will also including taking current-voltage readings of the emitter, as well as other diagnostics to determine performance. If completed, this would allow for the manufacturing of highly reliable, easily manufacturable electrospray thrusters, which can be built as extremely dense arrays capable of competing with hall thrusters and other advanced electric propulsion devices.

Appendix A

Fuse simulation layout and results

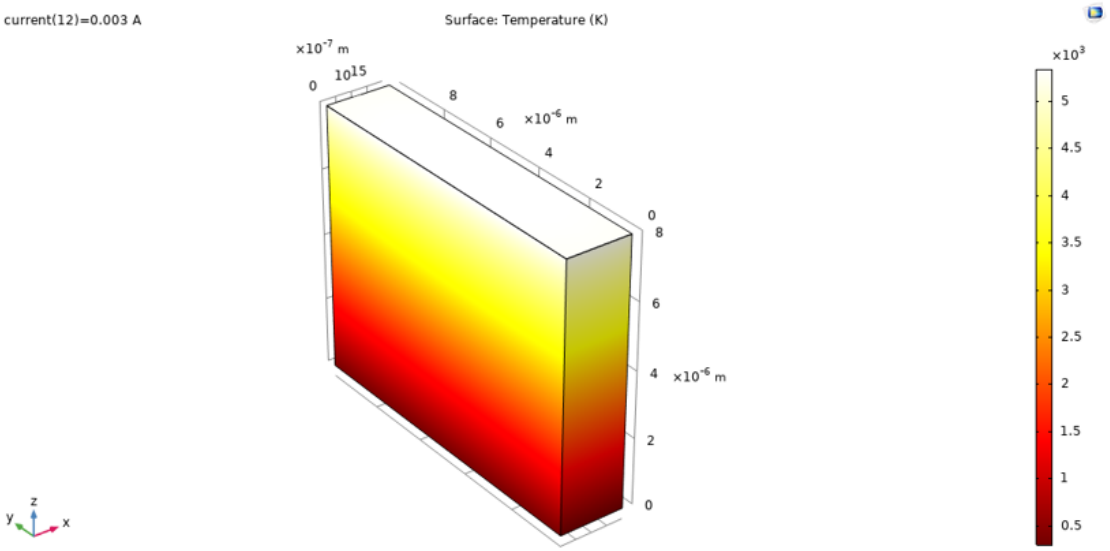

Figure A.1: COMSOL temperature simulation window for NiCr fuse with 3 mA current applied.

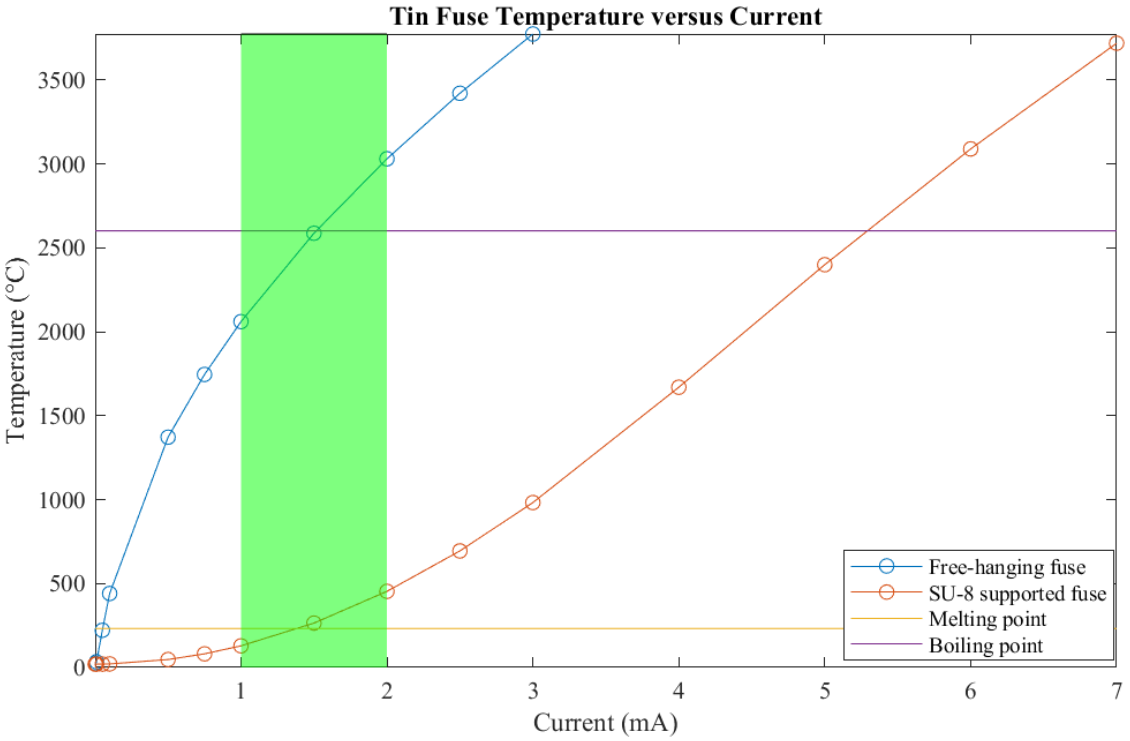

Figure A.2: COMSOL simulation of fuse temperature versus current for tin.

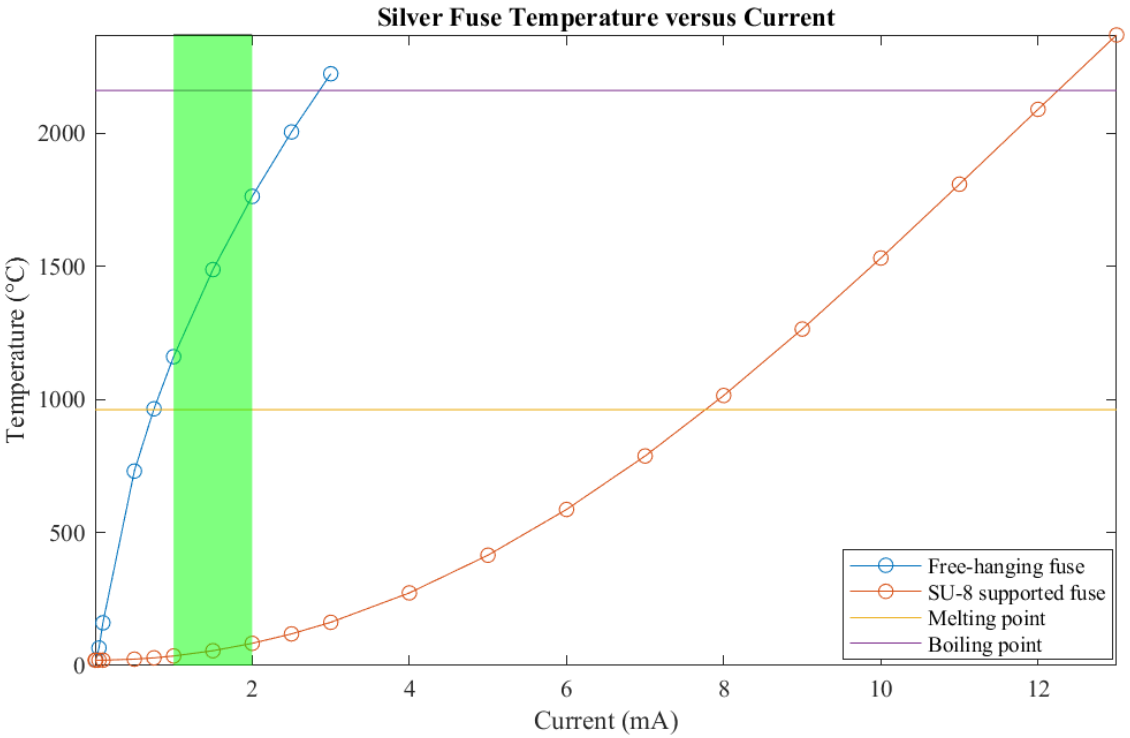

Figure A.3: COMSOL simulation of fuse temperature versus current for silver.

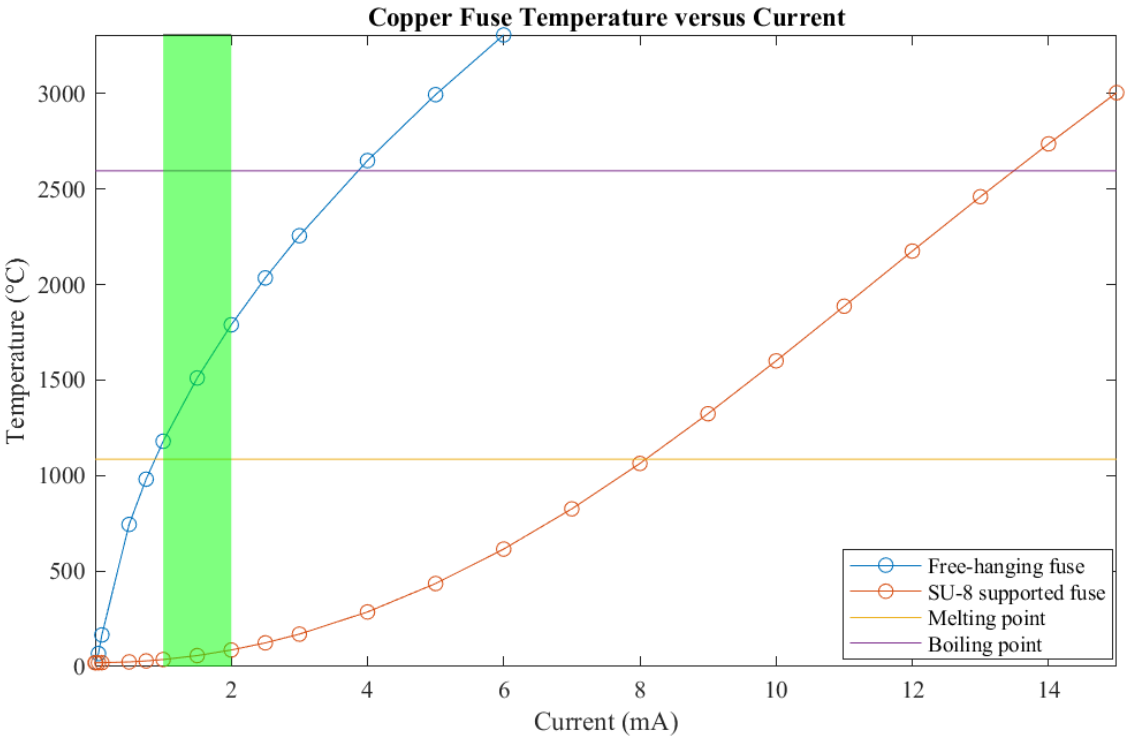

Figure A.4: COMSOL simulation of fuse temperature versus current for copper.

References

[1] L. Garrigues and P. Coche, "Electric propulsion: Comparisons between different concepts," *Plasma Physics and Controlled Fusion*, vol. 53, no. 12, p. 124 011, Nov. 2011, ISSN: 0741-3335. DOI: 10.1088/0741-3335/53/12/124011. URL: https://dx.doi.org/10.1088/0741-3335/53/12/124011.

[2] J. Mitterauer, "LIQUID METAL ION SOURCES AS THRUSTERS FOR ELECTRIC SPACE PROPULSION," *Le Journal de Physique Colloques*, vol. 48, no. C6, pp. C6–176, Nov. 1987, Publisher: EDP Sciences, ISSN: 0449-1947, 2777-3418. DOI: 10.1051/jphyscol:1987628. URL: http://dx.doi.org/10.1051/jphyscol:1987628.

[3] P. Lozano and M. Martinez-Sanchez, "Efficiency Estimation of EMI-BF4 Ionic Liquid Electrospray Thrusters," in *41st AIAA/ASME/SAE/ASEE Joint Propulsion Conference & Exhibit*, Tucson, Arizona: American Institute of Aeronautics and Astronautics, Jul. 2005, ISBN: 978-1-62410-063-5. DOI: 10.2514/6.2005-4388. URL: http://arc.aiaa.org/doi/abs/10.2514/6.2005-4388.

[4] D. Krejci, F. Mier-Hicks, C. Fucetola, P. Lozano, A. Hsu, and F. Martel, *Design and Characterization of a Scalable ion Electrospray Propulsion System*. Jul. 2015.

[5] A. M. Gañán-Calvo, J. M. López-Herrera, M. A. Herrada, A. Ramos, and J. M. Montanero, "Review on the physics of electrospray: From electrokinetics to the operating conditions of single and coaxial Taylor cone-jets, and AC electrospray," *Journal of Aerosol Science*, From Electro-Hydro-Dynamics of liquids for the production of charged droplets by Electro-Spray to applications for tailored Materials

(aerosols, powders, coatings) and Environment, vol. 125, pp. 32–56, Nov. 2018, ISSN: 0021-8502. DOI: 10.1016/j.jaerosci.2018.05.002. URL: https://www.sciencedirect.com/science/article/pii/S0021850217304305.

[6] I. Romero-Sanz, R. Bocanegra, J. Fernandez de la Mora, and M. Gamero-Castaño, "Source of heavy molecular ions based on Taylor cones of ionic liquids operating in the pure ion evaporation regime," *Journal of Applied Physics*, vol. 94, no. 5, pp. 3599–3605, Sep. 2003, ISSN: 0021-8979, 1089-7550. DOI: 10.1063/1.1598281. URL: http://aip.scitation.org/doi/10.1063/1.1598281.

[7] M. Wilm, "Principles of Electrospray Ionization," *Molecular & Cellular Proteomics : MCP*, vol. 10, no. 7, p. M111.009407, Jul. 2011, ISSN: 1535-9476. DOI: 10.1074/mcp.M111.009407. URL: https://www.ncbi.nlm.nih.gov/pmc/articles/PMC3134074/.

[8] A. M. Gañán-Calvo, "THE SURFACE CHARGE IN ELECTROSPRAYING: ITS NATURE AND ITS UNIVERSAL SCALING LAWS," *Journal of Aerosol Science*, vol. 30, no. 7, pp. 863–872, Aug. 1999, ISSN: 0021-8502. DOI: 10.1016/S0021-8502(98)00780-0. URL: https://www.sciencedirect.com/science/article/pii/S0021850298007800 (visited on 05/10/2024).

[9] J. Ziemer, "Performance of Electrospray Thrusters IEPC-2009-242," 2009. URL: https://www.semanticscholar.org/paper/Performance-of-Electrospray-Thrusters-IEPC-2009-242-Ziemer/ea656f3151d6df6d4aa47fbca7e070af6c6e7de2.

[10] C. Huang, J. Li, and M. Li, "Performance measurement and evaluation of an ionic liquid electrospray thruster," *Chinese Journal of Aeronautics*, Nov. 2021, ISSN: 1000-9361. DOI: 10.1016/j.cja.2021.10.030. URL: https://www.sciencedirect.com/science/article/pii/S1000936121004106.

[11] M. Gamero-Castano and V. Hruby, "Electrospray as a Source of Nanoparticles for Efficient Colloid Thrusters," *Journal of Propulsion and Power*, vol. 17, no. 5, pp. 977–987, Sep. 2001, Publisher: American Institute of Aeronautics and Astronautics, ISSN: 0748-4658. DOI: 10.2514/2.5858. URL: https://arc.aiaa.org/doi/10.2514/2.5858.

[12] J. Rojas-Herrera, I. Jivanescu, D. Freeman, D. Krejci, C. Fucetola, and P. Lozano, "Porous Materials for Ion-Electrospray Spacecraft Microengines," *Journal of Nanomechanics and Micromechanics*, vol. 7, no. 3, p. 04 017 006, Sep. 2017, Publisher: American Society of Civil Engineers, ISSN: 2153-5477. DOI: 10.1061/(ASCE)NM.2153-5477.0000121. URL: https://ascelibrary.org/doi/10.1061/%28ASCE%29NM.2153-5477.0000121.

[13] D. Krejci, F. Mier-Hicks, R. Thomas, T. Haag, and P. Lozano, "Emission Characteristics of Passively Fed Electrospray Microthrusters with Propellant Reservoirs," *Krejci*, Jul. 2017, Accepted: 2017-05-01T17:40:28Z Publisher: American Institute of Aeronautics and Astronautics, ISSN: 0022-4650. URL: https://dspace.mit.edu/handle/1721.1/108538.

[14] C. A. Spindt, "Microfabricated field-emission and field-ionization sources," *Surface Science*, vol. 266, no. 1, pp. 145–154, Apr. 1992, ISSN: 0039-6028. DOI: 10.1016/0039-6028(92)91012-Z. URL: https://www.sciencedirect.com/science/article/pii/003960289291012Z.

[15] A. Thuppul, P. L. Wright, A. L. Collins, J. K. Ziemer, and R. E. Wirz, "Lifetime Considerations for Electrospray Thrusters," *Aerospace*, vol. 7, no. 8, p. 108, Aug. 2020, Number: 8 Publisher: Multidisciplinary Digital Publishing Institute, ISSN: 2226-4310. DOI: 10.3390/aerospace7080108. URL: https://www.mdpi.com/2226-4310/7/8/108.

[16] N. Brikner and P. C. Lozano, "The role of upstream distal electrodes in mitigating electrochemical degradation of ionic liquid ion sources," *Applied Physics Letters*, vol. 101, no. 19, p. 193 504, Nov. 2012, Publisher: American Institute of Physics, ISSN: 0003-6951. DOI: 10.1063/1.4766293. URL: https://aip.scitation.org/doi/10.1063/1.4766293.

[17] K. J. Terhune, L. B. King, K. He, and J. Cumings, "Radiation-induced solidification of ionic liquid under extreme electric field," *Nanotechnology*, vol. 27, no. 37, p. 375 701, Sep. 2016, ISSN: 1361-6528. DOI: 10.1088/0957-4484/27/37/375701.

[18] V. K. Jain, A. Sidpara, R. Balasubramaniam, G. S. Lodha, V. P. Dhamgaye, and R. Shukla, "Micromanufacturing: A review—Part I," *Proceedings of the Institution of Mechanical Engineers, Part B: Journal of Engineering Manufacture*, vol. 228, no. 9, pp. 973–994, 2014, _eprint: https://doi.org/10.1177/0954405414539487. DOI: 10.1177/0954405414539487. URL: https://doi.org/10.1177/0954405414539487.

[19] T. J. Horn and D. O. L. A. Harrysson, "Overview of Current Additive Manufacturing Technologies and Selected Applications," *Science Progress*, vol. 95, no. 3, pp. 255–282, 2012, _eprint: https://doi.org/10.3184/003685012X13420984463047. DOI: 10.3184/003685012X13420984463047. URL: https://doi.org/10.3184/003685012X13420984463047.

[20] K. Sathish, S. S. Kumar, R. T. Magal, V. Selvaraj, V. Narasimharaj, R. Karthikeyan, G. Sabarinathan, M. Tiwari, and A. E. Kassa, "A Comparative Study on Subtractive Manufacturing and Additive Manufacturing," *Advances in Materials Science and Engineering*, vol. 2022, e6892641, Apr. 2022, Publisher: Hindawi, ISSN: 1687-8434. DOI: 10.1155/2022/6892641. URL: https://www.hindawi.com/journals/amse/2022/6892641/.

[21] T. Limongi, R. Schipani, A. Di Vito, *et al.*, "Photolithography and micromolding techniques for the realization of 3D polycaprolactone scaffolds for tissue engineering

applications," *Microelectronic Engineering*, Micro/Nano Fabrication 2014, vol. 141, pp. 135–139, Jun. 2015, ISSN: 0167-9317. DOI: 10.1016/j.mee.2015.02.030. URL: https://www.sciencedirect.com/science/article/pii/S0167931715000829.

[22] H. Miyajima and M. Mehregany, "High-aspect-ratio photolithography for MEMS applications," *Journal of Microelectromechanical Systems*, vol. 4, no. 4, pp. 220–229, Dec. 1995, Conference Name: Journal of Microelectromechanical Systems, ISSN: 1941-0158. DOI: 10.1109/84.475549. URL: https://ieeexplore.ieee.org/abstract/document/475549.

[23] J. T. M. Stevenson and A. M. Gundlach, "The application of photolithography to the fabrication of microcircuits," *Journal of Physics E: Scientific Instruments*, vol. 19, no. 9, p. 654, Sep. 1986, ISSN: 0022-3735. DOI: 10.1088/0022-3735/19/9/001. URL: https://dx.doi.org/10.1088/0022-3735/19/9/001.

[24] D. Bratton, D. Yang, J. Dai, and C. K. Ober, "Recent progress in high resolution lithography," *Polymers for Advanced Technologies*, vol. 17, no. 2, pp. 94–103, 2006, _eprint: https://onlinelibrary.wiley.com/doi/pdf/10.1002/pat.662, ISSN: 1099-1581. DOI: 10.1002/pat.662. URL: https://onlinelibrary.wiley.com/doi/abs/10.1002/pat.662.

[25] G. J. Leggett, "Scanning near-field photolithography—surface photochemistry with nanoscale spatial resolution," *Chem. Soc. Rev.*, vol. 35, no. 11, pp. 1150–1161, 2006, ISSN: 0306-0012, 1460-4744. DOI: 10.1039/B606706A. URL: http://xlink.rsc.org/?DOI=B606706A.

[26] J. del Barrio and C. Sánchez-Somolinos, "Light to Shape the Future: From Photolithography to 4D Printing," *Advanced Optical Materials*, vol. 7, no. 16, p. 1 900 598, 2019, _eprint: https://onlinelibrary.wiley.com/doi/pdf/10.1002/adom.201900598, ISSN: 2195-1071. DOI: 10.1002/adom.201900598. URL: https://onlinelibrary.wiley.com/doi/abs/10.1002/adom.201900598.

[27] W.-M. Yeh, D. E. Noga, R. A. Lawson, L. M. Tolbert, and C. L. Henderson, "Comparison of positive tone versus negative tone resist pattern collapse behavior," *Journal of Vacuum Science & Technology B, Nanotechnology and Microelectronics: Materials, Processing, Measurement, and Phenomena*, vol. 28, no. 6, C6S6–C6S11, Nov. 2010, ISSN: 2166-2746, 2166-2754. DOI: 10.1116/1.3518136. URL: https://pubs.aip.org/jvb/article/28/6/C6S6/581987/Comparison-of-positive-tone-versus-negative-tone.

[28] A. Anbari, H.-T. Chien, S. S. Datta, W. Deng, D. A. Weitz, and J. Fan, "Microfluidic Model Porous Media: Fabrication and Applications," *Small*, vol. 14, no. 18, p. 1 703 575, 2018, _eprint: https://onlinelibrary.wiley.com/doi/pdf/10.1002/smll.201703575, ISSN: 1613-6829. DOI: 10.1002/smll.201703575. URL: https://onlinelibrary.wiley.com/doi/abs/10.1002/smll.201703575.

[29] K.-i. Ohno, K. Tachikawa, and A. Manz, "Microfluidics: Applications for analytical purposes in chemistry and biochemistry," *ELECTROPHORESIS*, vol. 29, no. 22, pp. 4443–4453, 2008, _eprint: https://onlinelibrary.wiley.com/doi/pdf/10.1002/elps.200800121, ISSN: 1522-2683. DOI: 10.1002/elps.200800121. URL: https://onlinelibrary.wiley.com/doi/abs/10.1002/elps.200800121.

[30] S. L. Sjostrom, Y. Bai, M. Huang, Z. Liu, J. Nielsen, H. N. Joensson, and H. A. Svahn, "High-throughput screening for industrial enzyme production hosts by droplet microfluidics," *Lab on a Chip*, vol. 14, no. 4, pp. 806–813, Jan. 2014, Publisher: The Royal Society of Chemistry, ISSN: 1473-0189. DOI: 10.1039/C3LC51202A. URL: https://pubs.rsc.org/en/content/articlelanding/2014/lc/c3lc51202a.

[31] D.-S. Wang and S.-K. Fan, "Microfluidic Surface Plasmon Resonance Sensors: From Principles to Point-of-Care Applications," *Sensors*, vol. 16, no. 8, p. 1175, Aug. 2016, Number: 8 Publisher: Multidisciplinary Digital Publishing Institute, ISSN: 1424-8220. DOI: 10.3390/s16081175. URL: https://www.mdpi.com/1424-8220/16/8/1175.

[32] Tauseef-ur-Rehman, H. M. Ali, M. M. Janjua, U. Sajjad, and W.-M. Yan, "A critical review on heat transfer augmentation of phase change materials embedded with porous materials/foams," *International Journal of Heat and Mass Transfer*, vol. 135, pp. 649–673, Jun. 2019, ISSN: 0017-9310. DOI: 10.1016/j.ijheatmasstransfer.2019.02.001. URL: https://www.sciencedirect.com/science/article/pii/S0017931018349767.

[33] A. Walcarius, "Template-directed porous electrodes in electroanalysis," *Analytical and Bioanalytical Chemistry*, vol. 396, no. 1, pp. 261–272, Jan. 2010, ISSN: 1618-2650. DOI: 10.1007/s00216-009-3069-1. URL: https://doi.org/10.1007/s00216-009-3069-1.

[34] F. Javid, P. Wang, A. Shanian, and K. Bertoldi, "Architected Materials with Ultra-Low Porosity for Vibration Control," *Advanced Materials*, vol. 28, no. 28, pp. 5943–5948, 2016, _eprint: https://onlinelibrary.wiley.com/doi/pdf/10.1002/adma.201600052, ISSN: 1521-4095. DOI: 10.1002/adma.201600052. URL: https://onlinelibrary.wiley.com/doi/abs/10.1002/adma.201600052.

[35] D. V. Dudina, B. B. Bokhonov, and E. A. Olevsky, "Fabrication of Porous Materials by Spark Plasma Sintering: A Review," *Materials*, vol. 12, no. 3, p. 541, Jan. 2019, Number: 3 Publisher: Multidisciplinary Digital Publishing Institute, ISSN: 1996-1944. DOI: 10.3390/ma12030541. URL: https://www.mdpi.com/1996-1944/12/3/541.

[36] G. Ryan, A. Pandit, and D. P. Apatsidis, "Fabrication methods of porous metals for use in orthopaedic applications," *Biomaterials*, vol. 27, no. 13, pp. 2651–2670, May

2006, ISSN: 0142-9612. DOI: 10.1016/j.biomaterials.2005.12.002. URL: https://www.sciencedirect.com/science/article/pii/S0142961205011610.

[37] U. G. T. M. Sampath, Y. C. Ching, C. H. Chuah, J. J. Sabariah, and P.-C. Lin, "Fabrication of Porous Materials from Natural/Synthetic Biopolymers and Their Composites," *Materials*, vol. 9, no. 12, p. 991, Dec. 2016, Number: 12 Publisher: Multidisciplinary Digital Publishing Institute, ISSN: 1996-1944. DOI: 10.3390/ma9120991. URL: https://www.mdpi.com/1996-1944/9/12/991.

[38] Q. Fu, E. Saiz, and A. P. Tomsia, "Bioinspired Strong and Highly Porous Glass Scaffolds," *Advanced Functional Materials*, vol. 21, no. 6, pp. 1058–1063, 2011, _eprint: https://onlinelibrary.wiley.com/doi/pdf/10.1002/adfm.201002030, ISSN: 1616-3028. DOI: 10.1002/adfm.201002030. URL: https://onlinelibrary.wiley.com/doi/abs/10.1002/adfm.201002030.

[39] J. Maurath, J. Dittmann, N. Schultz, and N. Willenbacher, "Fabrication of highly porous glass filters using capillary suspension processing," *Separation and Purification Technology*, vol. 149, pp. 470–478, Jul. 2015, ISSN: 1383-5866. DOI: 10.1016/j.seppur.2015.06.022. URL: https://www.sciencedirect.com/science/article/pii/S1383586615300484.

[40] Y.-C. Tan, J. S. Fisher, A. I. Lee, V. Cristini, and A. P. Lee, "Design of microfluidic channel geometries for the control of droplet volume, chemical concentration, and sorting," *Lab on a Chip*, vol. 4, no. 4, pp. 292–298, Jul. 2004, Publisher: The Royal Society of Chemistry, ISSN: 1473-0189. DOI: 10.1039/B403280M. URL: https://pubs.rsc.org/en/content/articlelanding/2004/lc/b403280m.

[41] H.-S. Jang, M.-W. Cho, and D.-S. Park, "Micro Fluidic Channel Machining on Fused Silica Glass Using Powder Blasting," *Sensors*, vol. 8, no. 2, pp. 700–710, Feb. 2008, Number: 2 Publisher: Molecular Diversity Preservation International, ISSN: 1424-8220. DOI: 10.3390/s8020700. URL: https://www.mdpi.com/1424-8220/8/2/700.

[42] F. Kotz, P. Risch, K. Arnold, *et al.*, "Fabrication of arbitrary three-dimensional suspended hollow microstructures in transparent fused silica glass," *Nature Communications*, vol. 10, no. 1, p. 1439, Mar. 2019, Number: 1 Publisher: Nature Publishing Group, ISSN: 2041-1723. DOI: 10.1038/s41467-019-09497-z. URL: https://www.nature.com/articles/s41467-019-09497-z.

[43] Y. Liao and Y. Cheng, "Femtosecond Laser 3D Fabrication in Porous Glass for Micro- and Nanofluidic Applications," *Micromachines*, vol. 5, no. 4, pp. 1106–1134, Dec. 2014, Number: 4 Publisher: Multidisciplinary Digital Publishing Institute, ISSN: 2072-666X. DOI: 10.3390/mi5041106. URL: https://www.mdpi.com/2072-666X/5/4/1106.

[44] K. Sugioka, J. Xu, D. Wu, Y. Hanada, Z. Wang, Y. Cheng, and K. Midorikawa, "Femtosecond laser 3D micromachining: A powerful tool for the fabrication of microfluidic, optofluidic, and electrofluidic devices based on glass," *Lab on a Chip*, vol. 14, no. 18, pp. 3447–3458, Aug. 2014, Publisher: The Royal Society of Chemistry, ISSN: 1473-0189. DOI: 10.1039/C4LC00548A. URL: https://pubs.rsc.org/en/content/articlelanding/2014/lc/c4lc00548a.

[45] R. K. Jamal, F. A.-H. Mutlak, F. T. Ibrahim, and U. M. Nayef, "Synthesis of Ag2O films by pulsed laser deposited on porous silicon as gas sensor application," *Optik*, vol. 218, p. 164 971, Sep. 2020, ISSN: 0030-4026. DOI: 10.1016/j.ijleo.2020.164971. URL: https://www.sciencedirect.com/science/article/pii/S003040262030807X.

[46] M. Jeske, J. W. Schultze, M. Thönissen, and H. Münder, "Electrodeposition of metals into porous silicon," *Thin Solid Films*, European Materials Research Society 1994 Spring Conference, Symposium F: Porous Silicon and Related Materials, vol. 255, no. 1, pp. 63–66, Jan. 1995, ISSN: 0040-6090. DOI: 10.1016/0040-6090(94)05605-D. URL: https://www.sciencedirect.com/science/article/pii/004060909405605D.

[47] S. S. Khudiar, U. M. Nayef, and F. A. H. Mutlak, "Improvement of spectral responsivity of ZnO nanoparticles deposited on porous silicon via laser ablation in liquid," *Optik*, vol. 244, p. 167 530, Oct. 2021, ISSN: 0030-4026. DOI: 10.1016/j.ijleo.2021.167530. URL: https://www.sciencedirect.com/science/article/pii/S0030402621011499.

[48] J. Vinje, K. S. Beckwith, and P. Sikorski, "Electron Beam Lithography Fabrication of SU-8 Polymer Structures for Cell Studies," *Journal of Microelectromechanical Systems*, vol. 29, no. 2, pp. 160–169, Apr. 2020, Conference Name: Journal of Microelectromechanical Systems, ISSN: 1941-0158. DOI: 10.1109/JMEMS.2020.2967174. URL: https://ieeexplore.ieee.org/document/8982185.

[49] A. Delle Site, "The Vapor Pressure of Environmentally Significant Organic Chemicals: A Review of Methods and Data at Ambient Temperature," *Journal of Physical and Chemical Reference Data*, vol. 26, no. 1, pp. 157–193, Jan. 1997, ISSN: 0047-2689, 1529-7845. DOI: 10.1063/1.556006. URL: http://aip.scitation.org/doi/10.1063/1.556006.

[50] G. R. Parmar and N. N. Rao, "Emerging Control Technologies for Volatile Organic Compounds," *Critical Reviews in Environmental Science and Technology*, vol. 39, no. 1, pp. 41–78, Dec. 2008, Publisher: Taylor & Francis _eprint: https://doi.org/10.1080/10643380701413658, ISSN: 1064-3389. DOI: 10.1080/10643380701413658. URL: https://doi.org/10.1080/10643380701413658.

[51] C. Ma, V. Messina, C. Ryan, J. L. Rovey, Z. R. Putnam, M. F. Lembeck, and S. P. Berg, *Emission characterization of porous electrospray thrusters with actively controlled flow rate*, Conference or Workshop Item, Num Pages: 19, 2022. URL: https://eprints.soton.ac.uk/474346/.

[52] S. Whitaker, "Flow in porous media I: A theoretical derivation of Darcy's law," *Transport in Porous Media*, vol. 1, no. 1, pp. 3–25, Mar. 1986, ISSN: 1573-1634. DOI: 10.1007/BF01036523. URL: https://doi.org/10.1007/BF01036523.

[53] R. Sullivan and K. Hertel, "The permeability method for determining specific surface of fibers and powders," *Advances in colloid science*, vol. 1, pp. 37–80, 1942.

[54] X. Gallud and P. C. Lozano, "The emission properties, structure and stability of ionic liquid menisci undergoing electrically assisted ion evaporation," *Journal of Fluid Mechanics*, vol. 933, A43, Feb. 2022, ISSN: 0022-1120, 1469-7645. DOI: 10.1017/jfm.2021.988. URL: https://www.cambridge.org/core/product/identifier/S0022112021009885/type/journal_article.

[55] B. R. Reschke and A. T. Timperman, "A Study of Electrospray Ionization Emitters with Differing Geometries with Respect to Flow Rate and Electrospray Voltage," *Journal of The American Society for Mass Spectrometry*, vol. 22, no. 12, pp. 2115–2124, Dec. 2011, ISSN: 1879-1123. DOI: 10.1007/s13361-011-0251-4. URL: https://doi.org/10.1007/s13361-011-0251-4.

[56] W. H. Preece, "I. On the heating effects of electric currents. No. II," *Proceedings of the Royal Society of London*, vol. 43, no. 258-265, pp. 280–295, Jan. 1997, Publisher: Royal Society. DOI: 10.1098/rspl.1887.0133. URL: https://royalsocietypublishing.org/doi/10.1098/rspl.1887.0133.

[57] P. Lozano, M. Martínez-Sánchez, and J. M. Lopez-Urdiales, "Electrospray emission from nonwetting flat dielectric surfaces," *Journal of Colloid and Interface Science*, vol. 276, no. 2, pp. 392–399, Aug. 2004, ISSN: 0021-9797. DOI: 10.1016/j.jcis.2004.04.017.

[58] F. L. Kunze, T. Henning, and P. J. Klar, "3D micro printed capillary electrospray thruster with a fully modular integrated extraction electrode," *Journal of Electric*

Propulsion, vol. 3, no. 1, p. 3, Jan. 2024, ISSN: 2731-4596. DOI: 10.1007/s44205-023-00066-7. URL: https://doi.org/10.1007/s44205-023-00066-7.

[59] T. Shingu, M. Nagao, K. Murakami, H. Murata, S. Khumpuang, S. Hara, and Y. Takao, "Fabrication and Demonstration of SU-8 Based Emitter Arrays for Ionic Liquid Electrospray Thrusters," *Journal of Evolving Space Activities*, vol. 1, p. 30, 2023. DOI: 10.57350/jesa.30.

[60] A. Cisquella-Serra, M. Galobardes-Esteban, and M. Gamero-Castaño, "Scalable Microfabrication of Multi-Emitter Arrays in Silicon for a Compact Microfluidic Electrospray Propulsion System," *ACS Applied Materials & Interfaces*, vol. 14, no. 38, pp. 43 527–43 537, Sep. 2022, Publisher: American Chemical Society, ISSN: 1944-8244. DOI: 10.1021/acsami.2c12716. URL: https://doi.org/10.1021/acsami.2c12716.

[61] F. L. Kunze, T. Henning, and P. J. Klar, "Taking internally wetted capillary electrospray emitters to the sub-ten-micrometer scale with 3D microlithography," *AIP Advances*, vol. 11, no. 10, p. 105 315, Oct. 2021, ISSN: 2158-3226. DOI: 10.1063/5.0066619. URL: https://doi.org/10.1063/5.0066619.

[62] B. Bilenberg, S. Jacobsen, M. S. Schmidt, L. H. D. Skjolding, P. Shi, P. Bøggild, J. O. Tegenfeldt, and A. Kristensen, "High resolution 100kV electron beam lithography in SU-8," *Microelectronic Engineering*, Micro- and Nano-Engineering MNE 2005, vol. 83, no. 4, pp. 1609–1612, Apr. 2006, ISSN: 0167-9317. DOI: 10.1016/j.mee.2006.01.142. URL: https://www.sciencedirect.com/science/article/pii/S0167931706002206.

[63] B. Gorissen, C. Van Hoof, D. Reynaerts, and M. De Volder, "SU8 etch mask for patterning PDMS and its application to flexible fluidic microactuators," *Microsystems & Nanoengineering*, vol. 2, no. 1, pp. 1–5, Sep. 2016, Number: 1 Publisher: Nature Publishing Group, ISSN: 2055-7434. DOI: 10.1038/micronano.2016.45. URL: https://www.nature.com/articles/micronano201645.

[64] G. Rieveschl and F. E. Ray, "The Chemistry of Fluorene and its Derivatives.," *Chemical Reviews*, vol. 23, no. 2, pp. 287–389, Oct. 1938, ISSN: 0009-2665, 1520-6890. DOI: 10.1021/cr60075a002. URL: https://pubs.acs.org/doi/abs/10.1021/cr60075a002.

[65] S. Chung and S. Park, "Effects of temperature on mechanical properties of SU-8 photoresist material," *Journal of Mechanical Science and Technology*, vol. 27, no. 9, pp. 2701–2707, Sep. 2013, ISSN: 1738-494X, 1976-3824. DOI: 10.1007/s12206-013-0714-6. URL: http://link.springer.com/10.1007/s12206-013-0714-6.